Supersonic and Hypersonic Flows on 2D Unstructured Context: Part I

EDISSON SÁVIO DE GÓES MACIEL
IEA – Aeronautical Engineering Division
ITA – Aeronautical Technological Institute
Praça Mal. Eduardo Gomes, 50 – Vila das Acácias – São José dos Campos – SP – 12228-900
BRAZIL
edissonsavio@yahoo.com.br

Abstract: - In this work, numerical simulations involving supersonic and hypersonic flows on an unstructured context are analyzed. The Van Leer and the Radespiel and Kroll schemes are implemented on a finite volume formulation, using unstructured spatial discretization. The algorithms are implemented in their first and second order spatial accuracies. The second order spatial accuracy is obtained by a linear reconstruction procedure based on the work of Barth and Jespersen. Several non-linear limiters are studied, as well two types of linear interpolation, based on the works of Frink, Parikh and Pirzadeh and of Jacon and Knight. Two types of viscous calculation to the laminar case are compared. They are programmed considering the works of Long, Khan and Sharp and of Jacon and Knight. To the turbulent simulations, the Wilcox and Rubesin model is employed. The ramp problem to the inviscid simulations and the re-entry capsule problem to the hypersonic viscous simulations are studied. The results have demonstrated that the Van Leer algorithm yields the best results in terms of the prediction of the shock angle of the oblique shock wave in the ramp problem and the best value of the stagnation pressure at the configuration nose in the re-entry capsule problem. The convective time step is the best choice to accelerate the convergence of the numerical schemes, as reported by Maciel. In terms of turbulent results, the Wilcox and Rubesin model yields good results, proving the good capacity of this turbulence model in simulate high hypersonic flows. This paper is the first part of this work and is related to the theory and inviscid solutions. The second paper of this work is concerned with the laminar and turbulent viscous results.

Key-Words: - Supersonic and hypersonic flows; Unstructured discretization; Van Leer algorithm; Radespiel and Kroll algorithm; Wilcox and Rubesin turbulence model; Euler and Navier-Stokes equations, Two-dimensions.

1 Introduction

Conventional non-upwind algorithms have been used extensively to solve a wide variety of problems [1]. Conventional algorithms are somewhat unreliable in the sense that for every different problem (and sometimes, every different case in the same class of problems) artificial dissipation terms must be specially tuned and judicially chosen for convergence. Also, complex problems with shocks and steep compression and expansion gradients may defy solution altogether.

Upwind schemes are in general more robust but are also more involved in their derivation and application. Some upwind schemes that have been applied to the Euler equations are, for example, [2], [3] and [4]. Some comments about these methods are reported below:

[2] suggested an upwind scheme based on the flux vector splitting concept. This scheme considered the fact that the convective flux vector components could be written as flow Mach number polynomial functions, as main characteristic. Such polynomials presented the particularity of having the minor possible degree and the scheme had to satisfy seven basic properties to form such polynomials. This scheme was presented to the Euler equations in Cartesian coordinates and three-dimensions.

[3] proposed a new flux vector splitting scheme. They declared that their scheme was simple and its accuracy was equivalent and, in some cases, better than the [5] scheme accuracy in the solutions of the Euler and the Navier-Stokes equations. The scheme was robust and converged solutions were obtained so fast as the [5] scheme. The authors proposed the approximated definition of an advection Mach number at the cell face, using its neighbor cell values via associated characteristic velocities. This interface Mach number was so used to determine the upwind extrapolation of the convective quantities.

[4] emphasized that the [3] scheme had its merits of low computational complexity and low numerical diffusion as compared to other methods. They also mentioned that the original method had several deficiencies. The method yielded local pressure oscillations in the shock wave proximities, adverse mesh and flow alignment problems. In the [4] work, a hybrid flux vector splitting scheme, which alternated between the [3] scheme and the [2] scheme, in the shock wave regions, was proposed, assuring that resolution of strength shocks was clear and sharply defined.

Algorithms for solving the Euler equations using a perfect gas model on structured grids in two- and three-dimensions have become widespread in recent years ([6] and [7]). However, these algorithms have shown difficulties in predicting satisfactory results around complex geometries due to mesh irregularities. As a result, attention has turned to the development of solution algorithms on arbitrary unstructured grids. Impressive results have been obtained for a wide range of problems ([8] and [9]).

One problem associated with unstructured meshes is the increased difficulty in obtaining smooth higher order spatial approximations to state data at cell interfaces. Two methods have been used to obtain higher order accuracy on unstructured meshes. A method used by several researchers for cell vertex schemes ([10] and [11]) was applied to obtain higher order accuracy in a procedure analogous to MUSCL differencing on a structured mesh. A conventional structured mesh limiter can be employed in this scheme to obtain approximately monotone results near flow discontinuities. The second method, which was proposed by [9], linearly reconstructs the cell averaged data and imposes a monotone preserving limiter to achieve smooth results near flow discontinuities.

On an unstructured algorithm context, [12-13] has presented a work involving the numerical implementation of four typical algorithms of the Computational Fluid Dynamics community. The [2], [5], [14] and [15] algorithms were implemented and applied to the solution of aeronautical and of aerospace problems, in two-dimensions. The Euler equations in conservative form, employing a finite volume formulation and an unstructured spatial discretization, were solved. The [5] and the [15] schemes were flux difference splitting ones and more accurate solutions were expected. On the other hand, the [2] and the [14] schemes were flux vector splitting ones and more robustness properties were expected. The time integration was performed by a Runge-Kutta method of five stages. All four schemes were first order accurate in space and second order accurate in time. The steady state physical problems of the transonic flow along a convergent-divergent nozzle and of the supersonic flows along a ramp and around a blunt body were studied. The results have shown that the [5] scheme has presented the most severe pressure fields in the ramp and blunt body problems and the most accurate value of the stagnation pressure in the blunt body case. On the other hand, the [2] scheme has yielded the most accurate value of the shock angle in the ramp problem, while the [15] scheme has yielded the best value of the lift coefficient in the blunt body problem.

Following the studies of 2007, [16-17] has presented a work involving the numerical implementation of more three typical algorithms of the Computational Fluid Dynamics community. The [3], [4] and [18] algorithms were implemented and applied to the solution of aeronautical and aerospace problems, in two-dimensions. The Euler equations in conservative form, employing a finite volume formulation and an unstructured spatial discretization, were solved. The [18] scheme was a flux difference splitting one and more accurate solutions were expected. On the other hand, the [3] and [4] schemes were flux vector splitting ones and more robustness properties were expected. The time integration was performed by a Runge-Kutta method of five stages. All three schemes were first order accurate in space and second order accurate in time. The steady state physical problems of the transonic flow along a convergent-divergent nozzle, of the supersonic flows along a ramp and around a blunt body, and of the “cold gas” hypersonic flow around a double ellipse were studied. The results have shown that the [18] scheme presents the most severe pressure fields and the most accurate values of the stagnation pressure in the blunt body and in the double ellipse problems. On the other hand, the [3] scheme yields the best wall pressure distribution, in comparison with the experimental results, in the nozzle problem, whereas the [4] scheme yields the most accurate value of the shock angle in the ramp problem.

In relation to high resolution unstructured solutions, [19-20] has presented a work involving [3] and [4] schemes implemented on a finite volume context and using an upwind and unstructured spatial discretization to solve the Euler equations in the two-dimensional space. Both schemes were flux vector splitting ones. These schemes were implemented in their second order accuracy versions employing the linear reconstruction procedure of [9] and their results were compared with their first order accuracy versions and with theoretical results. Five

nonlinear flux limiters were studied: Barth and Jespersen (minmod like), Van Leer, Van Albada, Super Bee and β-limiter. The time integration used a Runge-Kutta method of five stages and was second order accurate. Both algorithms were accelerated to the steady state solution using a spatially variable time step procedure. This technique has proved excellent gains in terms of convergence ratio as reported in [21-22]. The algorithms were applied to the solution of the steady state physical problem of the supersonic flow along a compression corner. The results have shown that the [4] scheme using Barth and Jespersen, Van Leer, Van Albada and Super Bee nonlinear limiters presented the most accurate values to the shock angle of the oblique shock wave generated at the compression corner.

In 2010, [23-24] has implemented the [2] and [5] algorithms, on a finite volume context and employing an upwind and unstructured spatial discretization, to solve the Euler equations in two-dimensions. The [5] scheme was a flux difference splitting type algorithm, whereas the [2] scheme was a flux vector splitting type algorithm. Both algorithms were implemented in their second order versions, employing the [9] linear reconstruction procedure and their results were compared with their first order version solutions and theoretical results. Five non-linear flux limiters were studied: Barth and Jespersen (minmod), Van Leer, Van Albada, Super Bee and β-limiter. The Runge-Kutta method of five stages, second order accurate, was used to perform time integration. The steady state physical problem of the supersonic flow along a compression corner was studied. A spatially variable time step procedure was employed to accelerate the convergence of the numerical schemes to the steady state solution. Effective gains in terms of convergence acceleration were reported in [21-22]. The results have demonstrated that the [5] scheme in its second order version, using the Van Albada and Super Bee limiters, yielded the most accurate solutions.

In terms of turbulence studies, [25-26] has developed interesting investigation involving the turbulence models of [27] and [28] applied to the steady state problem of the supersonic flow along a ramp. The [29] and [30] algorithms were implemented and used to perform the numerical experiments. Both schemes were second order accurate in space and time. The [29] algorithm was a Lax-Wendroff type one and the time integration was performed in conjunction with the spatial discretization. The time integration was of predictor/corrector type. The [30] scheme was a symmetrical one and the time integration was performed according to a Runge-Kutta method. The Favre-averaged Navier-Stokes equations were solved, according to a finite volume formulation and on a structured spatial discretization context, and the [27] and [28] models were employed to describe the turbulence effects in the mean flow properties. A spatially variable time step procedure was employed to accelerate the convergence of [29] and [30] in the experiments. The results have demonstrated that the [30] algorithm predicts a pressure field more severe than that obtained by the [29] one, as the turbulent flow is studied, a more real situation, to both models. The pressure distribution along the ramp obtained by the [29] and [30] schemes presented the expected behavior in the turbulent solution generated by the [27] model, whereas the laminar solution simulated a weaker shock wave ahead of the ramp. In the case with the [28] model, only the solution obtained with the [30] scheme presented the expected pressure distribution behavior. In general terms, the [30] algorithm has presented the best solutions.

[31] has presented a work where the [2] flux vector splitting scheme was implemented, on a finite-volume context. The two-dimensional Favre-averaged Navier-Stokes equations were solved using an upwind discretization on a structured mesh. The [32] and [33] two-equation turbulence models were used in order to close the problem. The physical problems under studies were the low supersonic flow along a ramp and the moderate supersonic flow around a blunt body configuration. The implemented scheme used a MUSCL (Monotone Upstream-centered Schemes for Conservation Laws) procedure to reach second order accuracy in space. The time integration used a Runge-Kutta method of five stages and was second order accurate. The algorithm was accelerated to the steady state solution using a spatially variable time step. This technique has proved excellent gains in terms of convergence rate as reported in [21-22]. The results have demonstrated that the [33] model has yielded more critical pressure fields than the ones due to [32]. The shock angle of the oblique shock wave in the ramp problem and the stagnation pressure ahead of the blunt body configuration are better predicted by the [33] turbulence model.

In this work, numerical simulations involving supersonic and hypersonic flows on an unstructured context are analyzed. Based on the experiences performed in the structured and unstructured contexts aforementioned, the [2] and [4] algorithms are implemented on a finite volume formulation, using unstructured spatial discretization. The algorithms are implemented in their first and second

order spatial accuracies. The second order spatial accuracy is obtained by a linear reconstruction procedure based on the work of [9]. Several non-linear limiters are studied, as well two types of linear interpolation, based on the works of [18] and [34]. Two types of viscous calculation to the laminar case are compared. They are programmed considering the works of [34] and [35]. To the turbulent simulations, the k-ω^2 two-equation model of [33] is employed, considering the good experience observed by the present author in the structured case. The ramp problem to the inviscid simulations and the re-entry capsule problem to the hypersonic simulations are considered. A spatially variable time step procedure is implemented aiming to obtain fast convergence rates to the two algorithms, as reported by [21-22]. Five options of time step are described and studied. The results have demonstrated that the [2] algorithm yields the best solution in terms of the prediction of the shock angle of the oblique shock wave in the ramp problem and the best value of the stagnation pressure at the configuration nose of the re-entry capsule problem. In terms of turbulent results, the [33] model yields good results, proving the good capacity of this turbulence model to high hypersonic flows.

This work is divided in two parts:

Part I – It describes the theory to be studied in this work. It details the system equations, the numerical algorithms, the viscous formulation, the time step options, the initial and boundary conditions, etc.; the inviscid results are also presented in this part;

Part II – It describes the laminar and turbulent viscous results obtained by this work, analyzes them and makes comparisons.

2 Navier-Stokes Equations

The two-dimensional flow is modeled by the Navier-Stokes equations, which express the conservation of mass and energy as well as the momentum variation of a viscous, heat conducting and compressible media, in the absence of external forces. The Euler equations are obtained in the limiting case of an infinity Reynolds number or, in other words, neglecting the viscous vectors. So, their description is omitted. The integral form of these equations may be represented by:

$$\partial/\partial t \int_V Q dV + \int_S \left[\left(E_e - E_v\right) n_x + \left(F_e - F_v\right) n_y \right] dS + \int_V G dV = 0 , \quad (1)$$

where Q is written for a Cartesian system, V is the cell volume, n_x and n_y are components of the unity vector normal to the cell boundary, S is the flux area, E_e and F_e are the components of the convective, or Euler, flux vector, E_v and F_v are the components of the viscous, or diffusive, flux vector and G is the source term of the two-equation model. The vectors Q, E_e, F_e, E_v and F_v are, incorporating a k-ω^2 formulation, represented by:

$$Q = \begin{Bmatrix} \rho \\ \rho u \\ \rho v \\ e \\ \rho k \\ \rho s \end{Bmatrix}, E_e = \begin{Bmatrix} \rho u \\ \rho u^2 + p \\ \rho uv \\ (e+p)u \\ \rho ku \\ \rho su \end{Bmatrix}, F_e = \begin{Bmatrix} \rho v \\ \rho uv \\ \rho v^2 + p \\ (e+p)v \\ \rho kv \\ \rho sv \end{Bmatrix}, E_v = \begin{Bmatrix} 0 \\ t_{xx} + \tau_{xx} \\ t_{xy} + \tau_{xy} \\ f_x \\ \alpha_x \\ \beta_x \end{Bmatrix};$$

$$F_v = \begin{Bmatrix} 0 \\ t_{xy} + \tau_{xy} \\ t_{yy} + \tau_{yy} \\ f_y \\ \alpha_y \\ \beta_y \end{Bmatrix} \quad \text{and} \quad G = \begin{Bmatrix} 0 \\ 0 \\ 0 \\ 0 \\ G_k \\ G_s \end{Bmatrix}; \quad (2)$$

where the components of the viscous stress tensor are defined as:

$$t_{xx} = \left[2\mu_M \, \partial u/\partial x - 2/3\mu_M \left(\partial u/\partial x + \partial v/\partial y\right)\right]/\mathrm{Re};$$
$$t_{xy} = \mu_M \left(\partial u/\partial y + \partial v/\partial x\right)/\mathrm{Re};$$
$$t_{yy} = \left[2\mu_M \left(\partial v/\partial y\right) - 2/3\mu_M \left(\partial u/\partial x + \partial v/\partial y\right)\right]/\mathrm{Re}. \quad (3)$$

The components of the turbulent stress tensor (Reynolds stress tensor) are described by the following expressions:

$$\tau_{xx} = \left[2\mu_T \, \partial u/\partial x - 2/3\mu_T \left(\partial u/\partial x + \partial v/\partial y\right)\right]/\mathrm{Re} - 2/3\rho k \; ;$$
$$\tau_{xy} = \mu_T \left(\partial u/\partial y + \partial v/\partial x\right)/\mathrm{Re};$$
$$\tau_{yy} = \left[2\mu_T \, \partial v/\partial y - 2/3\mu_T \left(\partial u/\partial x + \partial v/\partial y\right)\right]/\mathrm{Re} - 2/3\rho k \; . \quad (4)$$

Expressions to f_x and f_y are given bellow:

$$f_x = \left(t_{xx} + \tau_{xx}\right)u + \left(t_{xy} + \tau_{xy}\right)v - q_x;$$

$$f_y = \left(t_{xy} + \tau_{xy}\right)u + \left(t_{yy} + \tau_{yy}\right)v - q_y, \quad (5)$$

where q_x and q_y are the Fourier heat flux components and are given by:

$$q_x = -\gamma/\mathrm{Re}\left(\mu_M/\mathrm{Pr}_L + \mu_T/\mathrm{Pr}_T\right)\partial e_i/\partial x;$$

$$q_y = -\gamma/\mathrm{Re}\left(\mu_M/\mathrm{Pr}_L + \mu_T/\mathrm{Pr}_T\right)\partial e_i/\partial y. \quad (6)$$

The diffusion terms related to the k-ω^2 equation are defined as:

$$\alpha_x = 1/\mathrm{Re}\left(\mu_M + \mu_T/\sigma_k\right)\partial k/\partial x;$$

$$\alpha_y = 1/\mathrm{Re}\left(\mu_M + \mu_T/\sigma_k\right)\partial k/\partial y; \quad (7)$$

$$\beta_x = 1/\mathrm{Re}\left(\mu_M + \mu_T/\sigma_s\right)\partial s/\partial x;$$

$$\beta_y = 1/\mathrm{Re}\left(\mu_M + \mu_T/\sigma_s\right)\partial s/\partial y. \quad (8)$$

In the above equations, ρ is the fluid density; u and v are Cartesian components of the velocity vector in the x and y directions, respectively; e is the total energy per unit volume; p is the static pressure; k is the turbulence kinetic energy; s is the second turbulent variable, which can be the rate of dissipation of the turbulence kinetic energy (k-ε model) or the square of the flow vorticity (k-ω^2 model). In the present study, $s = \omega^2$; the t's are viscous stress components; τ's are the Reynolds stress components; the q's are the Fourier heat flux components; G_k takes into account the production and the dissipation terms of k; G_s takes into account the production and the dissipation terms of ω^2; μ_M and μ_T are the molecular and the turbulent viscosities, respectively; Pr_L and Pr_T are the laminar and the turbulent Prandtl numbers, respectively; σ_k and σ_s are turbulence coefficients; γ is the ratio of specific heats; **Re** is the laminar Reynolds number, defined by:

$$\mathrm{Re} = \rho V_{REF} l_{REF}/\mu_M, \quad (9)$$

where V_{REF} is a reference flow velocity and l_{REF} is a configuration reference length. The internal energy of the fluid, e_i, is defined as:

$$e_i = e/\rho - 0.5\left(u^2 + v^2\right). \quad (10)$$

The molecular viscosity can be estimated by three options described in the sub-section 2.1. The Navier-Stokes equations are nondimensionalized in relation to the freestream density, ρ_∞, the freestream speed of sound, a_∞, and the freestream molecular viscosity, μ_∞. The system is closed by the state equation for a perfect gas:

$$p = (\gamma - 1)\left[e - 0.5\rho\left(u^2 + v^2\right) - \rho k\right], \quad (11)$$

considering the ideal gas hypothesis. The total enthalpy is given by $H = \left(e + p\right)/\rho$.

2.1 Molecular Viscosity – Models:

Three models to the molecular viscosity were studied in the laminar case:

(a) A constant value, equal to the nondimensionalized viscosity, which results in the value 1.0 to the molecular viscosity in the simulations;

(b) A variable molecular viscosity based on the empiric Sutherland formula:

$$\mu_M = bT^{1/2}/\left(1 + S/T\right), \quad (12)$$

where T is the absolute temperature (K), b = $1.458\text{x}10^{-6}$ Kg/(m.s.$K^{1/2}$) and S = 110.4 K, to the atmospheric air in the standard atmospheric conditions (see [36]).

(c) A variable molecular viscosity based on the [37] model:

$$\mu_M = kT^{0.72}, \quad (13)$$

where k = 1.0 is recommended by [37] and T is nondimensionalized by freestream speed of sound.

3 Van Leer and Radespiel and Kroll Algorithms

The space approximation of the integral Equation (1) to a triangular finite volume yields an ordinary differential equation system given by:

$$V_i\, dQ_i/dt = -C_i, \quad (14)$$

with C_i representing the net flux (residual) of the conservation of mass, conservation of momentum and conservation of energy in the volume V_i. The residual is calculated as:

$$C_i = F_1 + F_2 + F_3, \quad (15)$$

where F_l is the discrete convective minus diffusive flux at the interface "*l*". The cell volume on an unstructured context is defined by:

$$V_i = 0.5\left|\left(x_{n1}y_{n2} + y_{n1}x_{n3} + x_{n2}y_{n3}\right) - \left(x_{n3}y_{n2} + y_{n3}x_{n1} + x_{n2}y_{n1}\right)\right|, \quad (16)$$

with n_1, n_2 and n_3 being the nodes of a given triangular cell, defined in Fig. 1. Figure 1 exhibits the computational cell adopted for the simulations, as well its respective nodes, neighbors and flux interfaces.

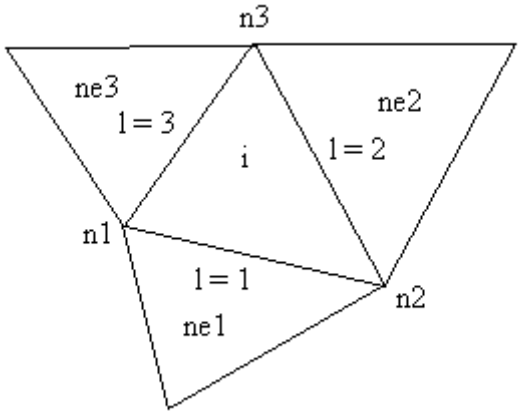

Figure 1: Schematic of a Cell and Its Neighbors, Nodes and Flux Interfaces.

The convective discrete flux calculated by the AUSM scheme (Advection Upstream Splitting Method) can be interpreted as a sum involving the arithmetical average between the right (R) and the left (L) states of the "*l*" cell face, multiplied by the interface Mach number, and a scalar dissipative term. The subscript "L" is associated to properties of a given "i" cell and the subscript "R" is associated to properties of the "ne" neighbor cell of "i". Hence, to the "*l*" interface:

$$F_l = |S|_l \left(\frac{1}{2} M_l \left(\begin{bmatrix} \rho a \\ \rho a u \\ \rho a v \\ \rho a H \\ \rho a k \\ \rho a s \end{bmatrix}_i + \begin{bmatrix} \rho a \\ \rho a u \\ \rho a v \\ \rho a H \\ \rho a k \\ \rho a s \end{bmatrix}_{ne} \right) - \frac{1}{2} \phi_l \left(\begin{bmatrix} \rho a \\ \rho a u \\ \rho a v \\ \rho a H \\ \rho a k \\ \rho a s \end{bmatrix}_{ne} - \begin{bmatrix} \rho a \\ \rho a u \\ \rho a v \\ \rho a H \\ \rho a k \\ \rho a s \end{bmatrix}_i \right) \right) + \begin{bmatrix} 0 \\ S_x p \\ S_y p \\ 0 \\ 0 \\ 0 \end{bmatrix}_l, \quad (17)$$

where $S_l = \left[S_x \quad S_y\right]_l^T$ defines the normal area vector to the "*l*" surface. The area components at this interface are defined by:

$$S_x^l = n_x^l S^l \quad \text{and} \quad S_y^l = n_y^l S^l. \quad (18)$$

The normal unity vector components, n_x^l and n_y^l, and the flux area of the "*l*" interface, S^l, are defined as:

$$n_x^l = \Delta y_l / \left(\Delta x_l^2 + \Delta y_l^2\right)^{0.5}, \; n_y^l = -\Delta x_l / \left(\Delta x_l^2 + \Delta y_l^2\right)^{0.5};$$

$$S^l = \left(\Delta x_l^2 + \Delta y_l^2\right)^{0.5}. \quad (19)$$

Expressions to Δx_l and Δy_l are given in Tab. 1. The quantity "a" represents the speed of sound, which is defined as:

$$a = \left(\gamma p/\rho - k\right)^{0.5}. \quad (20)$$

Interface	Δx_l	Δy_l
l = 1	$x_{n2} - x_{n1}$	$y_{n2} - y_{n1}$
l = 2	$x_{n3} - x_{n2}$	$y_{n3} - y_{n2}$
l = 3	$x_{n1} - x_{n3}$	$y_{n1} - y_{n3}$

Table 1: Values of Δx_l and Δy_l.

M_l defines the advection Mach number at the "*l*" face of the "i" cell, which is calculated according to [3] as:

$$M_l = M_L^+ + M_R^-, \quad (21)$$

where the separated Mach numbers $M^{+/-}$ are defined by the [2] formulas:

$$M^+ = \begin{cases} M, & \text{if } M \geq 1; \\ 0.25(M+1)^2, & \text{if } |M| < 1; \\ 0, & \text{if } M \leq -1; \end{cases}$$

$$M^- = \begin{cases} 0, & \text{if } M \geq 1; \\ -0.25(M-1)^2, & \text{if } |M| < 1; \\ M, & \text{if } M \leq -1. \end{cases} \quad (22)$$

M_L and M_R represent the Mach number associated with the left and right states, respectively. The advection Mach number is defined by:

$$M = \left(S_x u + S_y v\right) / \left(|S| a\right). \quad (23)$$

The pressure at the "*l*" face of the "i" cell is calculated by a similar way:

$$p_l = p_L^+ + p_R^-, \tag{24}$$

with $p^{+/-}$ denoting the pressure separation defined according to the [2] formulas:

$$p^+ = \begin{cases} p, & \text{if } M \geq 1; \\ 0.25p(M+1)^2(2-M), & \text{if } |M| < 1; \\ 0, & \text{if } M \leq -1; \end{cases}$$

$$p^- = \begin{cases} 0, & \text{if } M \geq 1; \\ 0.25p(M-1)^2(2+M), & \text{if } |M| < 1; \\ p, & \text{if } M \leq -1. \end{cases} \tag{25}$$

The definition of the dissipative term ϕ determines the particular formulation of the convective fluxes. The following choice corresponds to the [2] algorithm, according to [4]:

$$\phi_l = \phi_l^{VL} = \begin{cases} |M_l|, & \text{if } |M_l| \geq 1; \\ |M_l| + 0.5(M_R - 1)^2, & \text{if } 0 \leq M_l < 1; \\ |M_l| + 0.5(M_L + 1)^2, & \text{if } -1 < M_l \leq 0. \end{cases} \tag{26}$$

The above equations clearly show that to a supersonic cell face Mach number, the [2] scheme represents a discretization purely upwind, using either the left state or the right state to the convective terms and to the pressure, depending of the Mach number signal. This [2] scheme is first order accurate in space. The time integration is performed using an explicit Runge-Kutta method of five stages, second order accurate, and can be represented in generalized form by:

$$\begin{aligned} Q_i^{(0)} &= Q_i^{(n)} \\ Q_i^{(k)} &= Q_i^{(0)} - \alpha_k \Delta t_i \left[C\left(Q_i^{(k-1)}\right) / V_{i,j} + G\left(Q_{i,j}^{(k-1)}\right) \right], \\ Q_i^{(n+1)} &= Q_i^{(k)} \end{aligned} \tag{27}$$

with k = 1,...,5; $\alpha_1 = 1/4$, $\alpha_2 = 1/6$, $\alpha_3 = 3/8$, $\alpha_4 = 1/2$ and $\alpha_5 = 1$; and $C = F_1+F_2+F_3$.

The [4] scheme is described by Eqs. (16) to (25) and (27). The next step is the determination of the ϕ dissipative term. An hybrid scheme is proposed by [4], which combines the [2] scheme, better resolution at shock regions, and the [3] (AUSM) scheme, better resolution at background regions. Hence,

$$\phi_l = (1-\omega)\phi_l^{VL} + \omega\phi_l^{LS}, \tag{28}$$

with:

$$\phi_l^{VL} = \begin{cases} |M_l|, & \text{if } |M_l| \geq 1; \\ |M_l| + \frac{1}{2}(M_R - 1)^2, & \text{if } 0 \leq M_l < 1; \\ |M_l| + \frac{1}{2}(M_L + 1)^2, & \text{if } -1 < M_l \leq 0; \end{cases}$$

$$\phi_l^{LS} = \begin{cases} |M_l|, & \text{if } |M_l| \geq \tilde{\delta} \\ \dfrac{(M_l)^2 + \tilde{\delta}^2}{2\tilde{\delta}}, & \text{if } |M_l| < \tilde{\delta}, \end{cases} \tag{29}$$

where $\tilde{\delta}$ is a small parameter, $0 < \tilde{\delta} \leq 0.5$, and ω is a constant, $0 \leq \omega \leq 1$. In this work, the values used to $\tilde{\delta}$ and ω were: 0.2 and 0.5, respectively. The time integration follows the method described by Eq. (27). This scheme is first order accurate in space.

The gradients of the primitive variables to the viscous flux are calculated using the Green theorem, which considers that the gradient of a primitive variable is constant at the volume and that the volume integral which defines the gradient is replaced by a surface integral (see [35]). To the $\partial u/\partial x$ gradient, for example, it is possible to write:

$$\frac{\partial u}{\partial x} = \frac{1}{V}\int_V \frac{\partial u}{\partial x} dV = \frac{1}{V}\int_S u\left(\vec{n}_x \bullet d\vec{S}\right) = \frac{1}{V}\int_{S_x} u dS_x \cong$$

$$\frac{1}{V}\left[0.5(u_i + u_{ne1})S_{x_{i=1}} + 0.5(u_i + u_{ne2})S_{x_{i=2}} + 0.5(u_i + u_{ne3})S_{x_{i=3}}\right]. \tag{30}$$

4 Cell Centered Higher Order Correction

A piecewise linear redistribution of the cell averaged flow variables to obtain higher order accuracy while insuring that new extrema are not created in the reconstruction process is given by [9]:

$$Q(x,y) = Q(x_0,y_0) + \nabla Q \bullet r = Q(x_0,y_0) + Q_x[x - x_0] + Q_y[y - y_0], \tag{31}$$

where ***r*** is the vector from the cell center (x_0,y_0) to any point (x,y) in the cell, and ∇Q represents the solution gradient in the cell. Note that this equation

is simply the first order accurate Taylor approximation plus a higher order correction. With this approximation, the solution gradient ∇Q is constant in each cell and can be computed from

$$\nabla Q_i = \frac{1}{V_\Omega}\oint_\Omega (Q.n)d\Omega, \qquad (32)$$

where V_Ω is the volume contained in the path of integration. For the cell centered case, the path chosen passes through the centroids "*a*", "*b*" and "*c*" of the three surrounding cells "*ne1*", "*ne2*" and "*ne3*" of the given cell "i", respectively, as shown in Fig. 2.

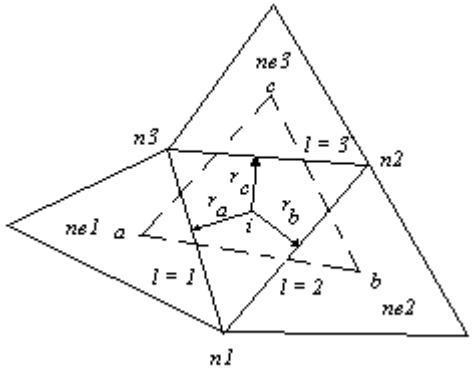

Figure 2: Integration Path for the Gradient Calculation.

The vector ∇Q represents the best estimate of the solution gradient in the cell computed from surrounding centroid data.

Consider a limited version of the linear function about the centroid of cell "i"

$$Q(x,y)_i = Q(x_0,y_0) + \Phi_i \nabla Q_i \bullet r_i, \quad \Phi_i \in [0,1]. \qquad (33)$$

To find the value of Φ_i, a monotonicity principle is enforced on the unlimited quantities $Q_{i_n} = Q(x_n,y_n)_i$ calculated in Eq. (31) at the faces of cell "i". It requires that the values computed at the faces must not exceed the maximum and minimum of neighboring centroid values, including the centroid value in cell "i", i.e., that

$$Q_i^{min} \le Q_{i_n} \le Q_i^{max}, \qquad (34)$$

where $Q_i^{min} = \min(Q_i, Q_{neighbors})$ and $Q_i^{max} = \max(Q_i, Q_{neighbors})$. Note that this definition differs from that of [38], but coincides with the monotonicity definition used recently by [39] for structured meshes in multi-dimensions. For linear reconstructions, extrema in $Q(x,y)_i$ occur at the vertices of the face and sufficient conditions for Eq. (33) can be easily obtained. The value Φ_i can now be calculated for each vertex "j" of cell "i" as

$$z = \begin{cases} \dfrac{Q_i^{max} - Q_i}{Q_j - Q_i}, & \text{if} \quad Q_j - Q_i > 0; \\ \dfrac{Q_i^{min} - Q_i}{Q_j - Q_i}, & \text{if} \quad Q_j - Q_i < 0; \quad \overline{\Phi}_{i_j} = \min(1,z), \\ 1, & \text{if} \quad Q_j - Q_i = 0; \end{cases} \qquad (35)$$

with $\Phi_i = \min(\overline{\Phi}_{i_1}, \overline{\Phi}_{i_2}, \overline{\Phi}_{i_3})$, where "j" is the index of each vertex defining cell "i". New limited values for Q_i at each of the faces of cell "i" are then calculated from Eq. (33) using the value of Φ_i calculated for the cell. Following this procedure guarantees that the linearly reconstructed state variables satisfy the monotonicity principle when evaluated anywhere within a face. The nonlinear limiter described by Eq. (35) is of a minmod type. Other limiters are presented below and were studied in this work. The definitions of these limiters are presented in [40].

- Van Leer non-linear limiter:

$$\overline{\Phi}_{i_j} = \frac{z + |z|}{1 + z}; \qquad (36)$$

- Van Albada non-linear limiter:

$$\overline{\Phi}_{i_j} = \frac{z + z^2}{1 + z^2}; \qquad (37)$$

- Super Bee non-linear limiter:

$$\overline{\Phi}_{i_j} = \max[0, \min(2z,1), \min(z,2)]; \qquad (38)$$

- β-limiter:

$$\overline{\Phi}_{i_j} = \max[0, \min(\beta z,1), \min(z,\beta)], \qquad (39)$$

where "z" is the ratio of differences of the vector of conserved variables, defined according to Eq. (35), and β assumes values from 1.0 to 2.0, being 1.5 the value adopted in this work.

5 Laminar Viscous Flux – Jacon and Knight Procedure

The contribution to C_i from the viscous fluxes and heat transfer on face "k" is obtained from application of Gauss' Theorem (see [41]) to the quadrilateral defined by the centroids of the cells adjacent to face "k" and the two nodes defining the endpoints (see Fig. 3). For any function f(x,y),

$$\frac{\partial f}{\partial x} = \frac{1}{V}\int_{\partial V} f n_x dA, \qquad (40)$$

where V and ∂V are the volume and surface of the quadrilateral *abcd*, respectively, and n_x is the component of the outwards normal in the x direction. A similar equation is obtained for $\partial f/\partial y$. The values of $\partial f/\partial x$ and $\partial f/\partial y$ are evaluated at midpoint *p* of Fig. 3. The values of Q at the nodes are needed both the reconstruction process and the laminar viscous terms and are obtained by second order interpolation of Q from those cells sharing the node (see [42]):

$$Q_j = \sum_{cells} \omega_i Q_i \Big/ \sum_{cells} \omega_i, \qquad (41)$$

where Q_j denotes the Q at node j, Q_i denotes Q at the centroid of cell "i" which shares the node j, the sum is over all cells sharing the node (x_j,y_j), and ω_i are dimensionless weights.

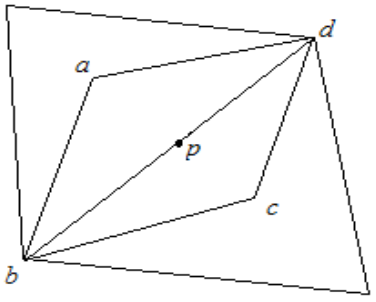

Figure 3: Quadrilateral Employed for Determination of Viscous Fluxes.

In the present study, two forms of evaluating ω_i are studied: the first proposed by [34] and the second due to [18]. In the first method, ω_i is given by:

$$\omega_i = 1 + \lambda_x (x_i - x_j) + \lambda_y (y_i - y_j), \qquad (42)$$

with:

$$\lambda_x = (I_{xy}R_y - I_{yy}R_x)/(I_{xx}I_{yy} - I_{xy}^2); \qquad (43)$$

$$\lambda_y = (I_{xy}R_x - I_{xx}R_y)/(I_{xx}I_{yy} - I_{xy}^2); \qquad (44)$$

$$R_x = \sum_{cells}(x_i - x_j); \quad R_y = \sum_{cells}(y_i - y_j); \qquad (45)$$

$$I_{xx} = \sum_{cells}(x_i - x_j)^2; \quad I_{yy} = \sum_{cells}(y_i - y_j)^2; \qquad (46)$$

$$I_{xy} = \sum_{cells}(x_i - x_j)(y_i - y_j). \qquad (47)$$

In the second method, ω_i is given by:

$$\omega_i = \left[(x_i - x_j)^2 + (y_i - y_j)^2\right]^{0.5}, \qquad (48)$$

being (x_i,y_i) the centroid coordinates of cell "i".

6 Wilcox and Rubesin Model to Turbulent Flow

In this work, the k-ω^2 model of [33] is studied, where $s = \omega^2$. To define the turbulent viscosity, it is necessary to define the turbulent Reynolds number:

$$Re_T = k/(\nu_M \omega), \qquad (49)$$

with: $\nu_M = \mu_M/\rho$ and ω defined as $\sqrt{s} = \sqrt{\omega^2}$. It needs to define a D damping factor:

$$D = 1 - \alpha e^{(-Re_T)}, \qquad (50)$$

with: α a constant to be defined. The turbulent viscosity is expressed in terms of k and ω as:

$$\mu_T = Re\, D\rho k/\omega. \qquad (51)$$

The source term denoted by G in the governing equation contains the production and dissipation terms of k and ω^2. To the [33] model, the G_k and G_{ω^2} terms have the following expressions:

$$G_k = -P_k - D_k \quad \text{and} \quad G_{\omega^2} = -P_{\omega^2} - D_{\omega^2}, \qquad (52)$$

where:

$$P = \left(\frac{\partial u}{\partial y} + \frac{\partial v}{\partial x}\right)\frac{\partial u}{\partial y}, \; P_k = \left(\frac{DP}{\omega^2}\right)\rho\omega k \Big/ Re;$$

$$D_k = \left[-\frac{2}{3}\left(\frac{\partial u}{\partial x} + \frac{\partial v}{\partial y}\right)\Big/\omega - \beta^*\right]\rho\omega k \Big/ Re; \qquad (53)$$

$$P_{\omega^2} = \left(\frac{\gamma_\infty EP}{\omega^2}\right)\rho\omega^3 \Big/ Re\,,$$

$$D_{\omega^2} = \left\{-\frac{2}{3}\gamma_\infty\left(\frac{\partial u}{\partial x}+\frac{\partial v}{\partial y}\right)\Big/\omega - \left[\beta + \frac{2}{\sigma_{\omega^2}}\left(\frac{\partial\sqrt{k/\omega^2}}{\partial y}\right)^2\right]\right\}\rho\omega^3 \Big/ Re\,, \tag{54}$$

with the second damping factor E defined as:

$$E = 1 - \alpha e^{(-0.5 Re_T)}. \tag{55}$$

The closure coefficients adopted to the [33] model assume the following values: $\alpha = 0.99174$; $\beta = 0.15$; $\beta^* = 0.09$; $\sigma_k = 2.0$; $\sigma_{\omega^2} = 2.0$; $\gamma_\infty = 0.9$; $Prd_L = 0.72$; $Prd_T = 0.9$.

7 Unstructured Triangulation

An unstructured discretization of the calculation domain is usually recommended to complex configurations, due to the easily and efficiency that such domains can be discretized ([30], [43] and [44]). However, the unstructured mesh generation question will not be studied in this work. The unstructured meshes generated in this work were structured created and posteriorly the connectivity, neighboring, node coordinates and ghost tables were built in a pre-processing stage.

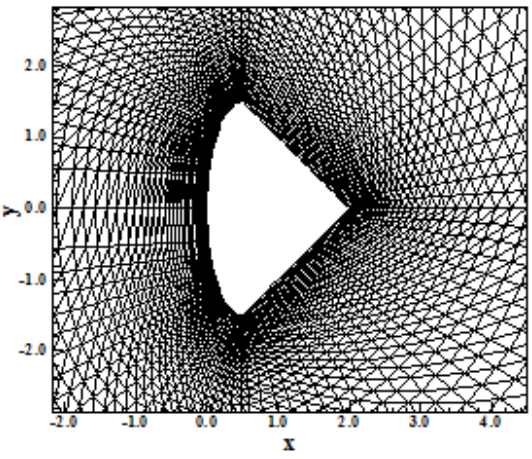

Figure 4: Triangulation in the Same Sense (SS).

A study involving two types of domain triangulation is performed. In the first case, the mesh is generated with the triangles created in the same sense (see Fig. 4). In the second case, the triangles generated in one row is in a specific sense and in the above row is in an opposite sense (see Fig. 5), originating a mesh with more regular geometrical properties. It is important to emphasize that in the second method, the number of lines should be odd. These triangulation options are studied in all cases: inviscid, laminar and turbulent.

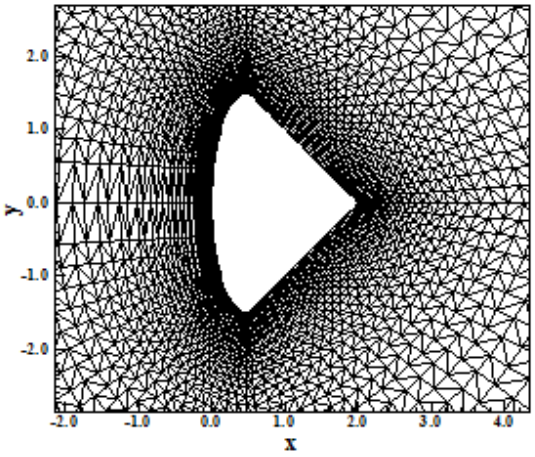

Figure 5: Triangulation in Alternate Sense (AS).

8 Time Step Options

8.1 Spatially Variable Time Steps

The basic idea of the spatially variable time step procedure consists in keeping constant the CFL number in all calculation domain, allowing, hence, the use of appropriated time steps to each specific mesh region during the convergence process. In this work, two options of spatially variable time step calculated at each iteration were studied and are described below:

(a) Convective time step:

According to the definition of the CFL number, it is possible to write:

$$\Delta t_i = CFL(\Delta s)_i / c_i\,, \tag{55}$$

where: CFL is the "Courant-Friedrichs-Lewy" number to provide numerical stability to the scheme; $c_i = \left[\left(u^2 + v^2\right)^{0.5} + a\right]_i$ is the maximum characteristic velocity of information propagation in the calculation domain; and $(\Delta s)_i$ is a characteristic length of information transport. Considering a finite volume context, $(\Delta s)_i$ is chosen as the minor value

found between the minor centroid distance, involving the "i" cell and a neighbor, and the minor cell side length.

(b) Convective + diffusive time step:

To a viscous simulation and according to the work of [37], it is possible to write:

$$\Delta t_i = \left(\frac{CFL(\Delta t_c \Delta t_v)}{\Delta t_c + \Delta t_v} \right)_i , \quad (56)$$

with Δt_c being the convective time step and Δt_v being the viscous time step. These quantities are defined as:

$$(\Delta t_c)_i = \frac{V_i}{(\lambda_c)_i} , \ (\lambda_c)_i = \max\left(\lambda_{l=1}^{max}, \lambda_{l=2}^{max}, \lambda_{l=3}^{max}\right);$$

$$\lambda_{int}^{max} = \left(|u_{int} n_x + v_{int} n_y| + a_{int}\right) S_{int}; \quad (57)$$

$$(\Delta t_v)_i = K_v \frac{V_i}{(\lambda_v)_i} , \ (p1)_i = \frac{\gamma^{3/2} M_\infty}{(Re\, Prd_L) V_i}; \quad (58a)$$

$$(p2)_i = \frac{\mu_{l=1}}{\rho_{l=1}} S_{l=1}^2 + \frac{\mu_{l=2}}{\rho_{l=2}} S_{l=2}^2 + \frac{\mu_{l=3}}{\rho_{l=3}} S_{l=3}^2, \ (\lambda_v)_i = (p1 \times p2)_i , \quad (58b)$$

where interface properties are calculated by arithmetical average, M_∞ is the freestream Mach number, μ is the fluid molecular viscosity and K_v is equal to 0.25, as recommended by [37].

8.2. Geometrical Time Steps

Following the idea of keeping an appropriated time step to each mesh region, it is proposed in this work two options of time step which depend of the studied mesh region. They are called "geometrical" time steps because depend mainly of the cell volume in a given region. They are described below:

(a) Geometrical time step – Option 1:

This time step is defined as:

$$\Delta t_i = \left(\frac{dt_0}{1 + 1/V_i} \right)_i , \text{ with } dt_0 = CFL. \quad (59)$$

(b) Geometrical time step – Option 2:
This time step option is an improvement of Eq. (59) and is defined as:

$$\Delta t_i = \left[\frac{dt_0}{1 + (1/V_i)^{exp}} \right]_i , \text{ with } dt_0 = CFL \text{ and } exp = 1/2 \text{ or } 1/3. \quad (60)$$

8.3. Constant Time Steps

In this case, the time step is defined as the minimum one calculated by Eq. (55), at the first iteration, and is keeping constant along all convergence process.

9 Initial and Boundary Conditions

9.1 Initial Condition

Freestream values, at all grid cells, are adopted for all flow properties as initial condition, as suggested by [30] and [45]. Therefore, the vector of conserved variables is defined as:

$$Q_i = \left\{ 1 \quad M_\infty \cos\alpha \quad M_\infty \sin\alpha \quad \frac{1}{\gamma(\gamma-1)} + 0.5 M_\infty^2 \quad k_\infty \quad \omega_\infty^2 \right\}^T , \quad (61)$$

where k_∞ is the freestream turbulent kinetic energy and ω_∞ is the freestream turbulent vorticity. These parameters assumes the following values in the present work: $k_\infty = 1.0 \times 10^{-6}$ and $\omega_\infty = (10 u_\infty / l_{REF})^2$, with u_∞ being the freestream u Cartesian component of velocity and l_{REF} being a characteristic length, the same adopted in the definition of the Reynolds number.

9.2. Boundary Conditions

The boundary conditions are basically of five types: solid wall, entrance, exit, far field and continuity. These conditions are implemented with the help of ghost cells.

9.2.1 Wall Condition

Considering the inviscid case, this condition imposes the flow tangency at the solid wall. It is satisfied considering the wall tangent velocity component of the ghost volume as equals to the respective velocity component of its real neighbor cell. At the same way, the wall normal velocity component of the ghost cell is equaled in value, but

with opposite signal, to the respective velocity component of the real neighbor cell. On the other hand, in the viscous case, it imposes the non-permeability and non-slip wall conditions. Therefore, the tangent velocity component of the ghost volume at wall has the same magnitude as the respective velocity component of its real neighbor cell, but opposite signal. In the same way, the normal velocity component of the ghost volume at wall is equal in value, but opposite in signal, to the respective velocity component of its real neighbor cell. These procedures lead to the following expressions to u_{ghost} and v_{ghost}, in each case:

$$\left.\begin{aligned} u_{ghost} &= \left(n_y^2 - n_x^2\right)u_{real} - (2n_x n_y)v_{real} \\ v_{ghost} &= -(2n_x n_y)u_{real} + \left(n_x^2 - n_y^2\right)v_{real} \end{aligned}\right\} \Rightarrow \text{Inviscid case ;} \quad (62)$$

$$\left.\begin{aligned} u_{ghost} &= -u_{real} \\ v_{ghost} &= -v_{real} \end{aligned}\right\} \Rightarrow \text{ Viscous case.} \quad (63)$$

The pressure gradient normal to the wall is assumed to be equal to zero, following an inviscid formulation or a boundary-layer like condition. The same hypothesis is applied to the temperature gradient normal to the wall, considering adiabatic wall. The ghost volume density and pressure are extrapolated from the respective values of the real neighbor volume (zero order extrapolation), with these two conditions. The total energy is obtained by the state equation of a perfect gas.

To the k-ω^2 model, the turbulent kinetic energy and the turbulent vorticity at the wall ghost volumes are determined by the following expressions:

$$k_{ghost} = 0.0 \quad \text{and} \quad \omega_{ghost} = \left[(38/3\nu_M)/(\beta d_n^2)\right]^2, \quad (64)$$

where β assumes the value 3/40 and d_n is the distance of the first centroid point to the wall.

9.2.2 Entrance Condition

The entrance condition considers subsonic and supersonic flow. They are detailed below:

(a) Subsonic flow: Five properties are specified and one extrapolated. This approach is based on information propagation analysis along characteristic directions in the calculation domain (see [45]). In other words, for subsonic flow, five characteristic propagate information point into the computational domain. Thus five flow properties must be fixed at the inlet plane. Just one characteristic line allows information to travel upstream. So, one flow variable must be extrapolated from the grid interior to the inlet boundary. The pressure was the extrapolated variable from the real neighbor volumes, for all studied problems. Density and velocity components adopted values of freestream flow. To the k-ω^2 model, the turbulence kinetic energy and the turbulence vorticity assume the values of the initial condition (freestream flow). The total energy is determined by the state equation of a perfect gas.

(b) Supersonic flow: In this case no information travels upstream; therefore all variables are fixed with their freestream values.

9.2.3 Exit Condition

Again, two flow situations are analyzed. They are detailed below:

(a) Subsonic flow: Five characteristic propagate information outward the computational domain. Hence, the associated variables should be extrapolated from interior information. The characteristic direction associated to the "(q_{normal}-a)" velocity should be specified because it point inward to the computational domain (see [45]). In this case, the ghost volume pressure is specified from its initial value. Density, velocity components, the turbulence kinetic energy and the turbulence vorticity are extrapolated. The total energy is obtained from the state equation of a perfect gas.

(b) Supersonic flow: All variables are extrapolated from interior grid cells, as no flow information can make its way upstream. In other words, nothing can be fixed.

9.2.4 Far field condition

This condition is only needed to the turbulent variables, once the far field is also an entrance and/or exit boundary. The mean flow kinetic energy is assumed to be $K = 0.5u^2$ and the turbulence kinetic energy at the far field adopts the value k_{ff} = 0.01K, or 1% of K. The turbulence vorticity is determined by its freestream value.

9.2.5 Continuity condition

This condition requires the flow continuity at the trailing edge of the re-entry capsule (Kutta condition). It is done considering the vector of conserved variables at the trailing edge lower-surface as equal to the vector of conserved variables at the trailing edge upper-surface.

10 Inviscid Results

Two problems were studied in this work, namely: the inviscid supersonic flow along a ramp geometry and the viscous hypersonic flow around a re-entry capsule geometry. In this part of the present work, the inviscid supersonic flow along a ramp is studied. The ramp configuration is detailed as also the type of boundary contours. These configuration characteristics are described in Figs. 6 and 7.

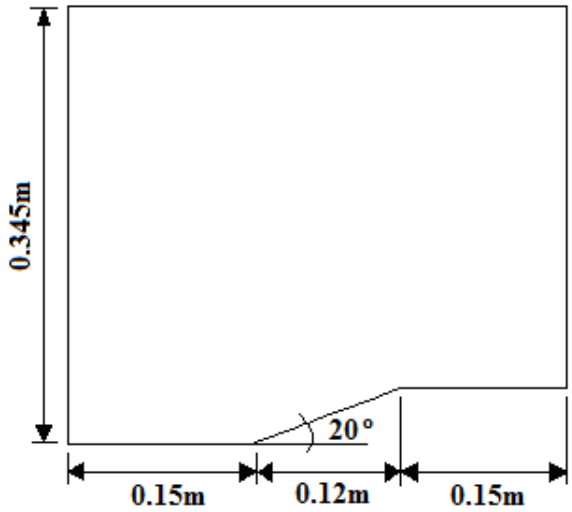

Figure 6: Ramp Configuration.

The re-entry capsule is detailed and studied in [46]. Numerical experiments were run on a Notebook computer with dual core processor of 2.13GHz of clock and 4.0 GB of RAM. The criterion adopted to reach the steady state was to consider a reduction of three (3) orders of magnitude in the value of the maximum residual in the calculation domain, a typical CFD community criterion. The maximum residual is defined as the maximum value obtained from the discretized equations in the overall domain, considering all conservation equations.

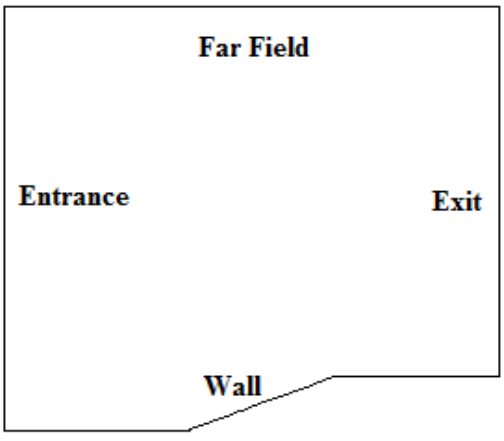

Figure 7: Ramp Computational Domain.

The necessary tables to run the unstructured algorithms are generated in a pre-process stage. The initial conditions to the ramp problem are described in Tab. 2.

Problem:	Property:	Value:
Ramp	Freestream Mach, M_∞	2.0
	Attack angle, °	0.0
	Ratio of specific heats, γ	1.4

Table 2: Initial Conditions to the Studied Problem.

The number of cells and nodes for the ramp problem are presented in Tab. 3. A mesh of 61x61 nodes, in a finite difference context, is employed.

Problem:	Number of triangular cells:	Number of nodes:
Ramp	7,200	3,721

Table 3: Cells and Nodes of the Mesh.

Figures 8 and 9 exhibit the meshes employed in the calculation of the inviscid flow to the ramp calculation. Figure 8 shows the mesh oriented in the same sense (clockwise sense) and Fig. 9 exhibits the mesh oriented in the alternate sense (one row is in clockwise sense and the following is in the counter-clockwise sense). Both cases are analyzed in the inviscid and viscous cases.

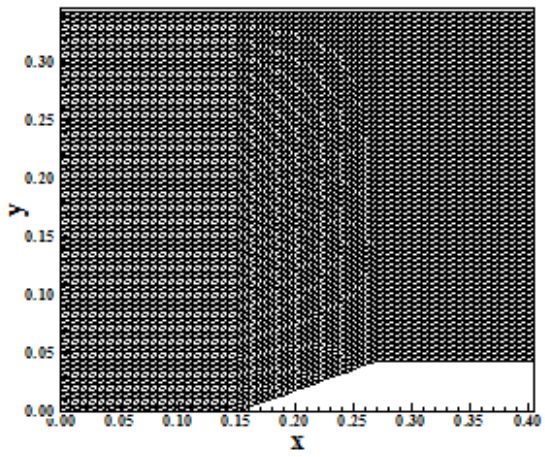

Figure 8: Ramp Mesh in the Same Sense (SS).

From now on, the term “SS” represents the first type of mesh, or better, represent the mesh oriented in the

same sense, whereas the term "AS" represents the second type of mesh, the mesh oriented in the clockwise sense in one row and in the counter-clockwise sense in the following row.

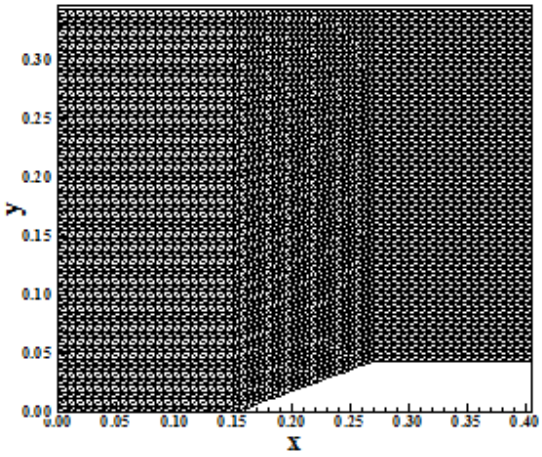

Figure 9: Ramp Mesh in the Alternate Sense (AS).

The first results present the first order solution obtained by the [2] and [4] algorithms. The inviscid supersonic flow along a ramp is employed to test the capacity of the algorithms to simulate inviscid supersonic flow, in both SS and AS cases. In section **10.2.**, this same test case is studied by the second order versions of [2] and [4], in both SS and AS cases.

10.1 First Order Inviscid Solutions – Ramp Problem

Figures 10 to 13 exhibit the density field obtained by [2] and [4] in SS and AS cases. The density field generated by the [2] algorithm in AS case is denser than the other fields. Good solution quality is observed in all four cases, mainly to the AS cases, which do not present shock oscillations in the density contours. However, as observed, the AS cases present solutions with a "cut out" effect, which damages lightly the quality solution. Both algorithms present this behavior to the AS case, which indicates that it is a problem of the mesh discretization and not of the numerical schemes.

Figures 14 to 17 show the pressure field obtained by [2] and [4], in the SS and AS cases, along the ramp geometry. The most severe pressure field is obtained by the [4] algorithm, in the SS case.

Figures 18 to 21 exhibit the Mach number field obtained by [2] and [4] in the cases SS and AS. As can see, they do not present Mach number oscillations and are clear. It is possible to note that the most intense Mach number field is due to [2] in the AS case. The smallest shock wave thickness is observed in both AS solutions.

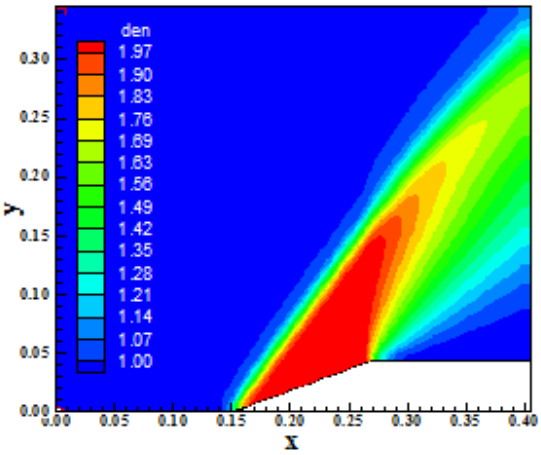

Figure 10: Density Field ([2] – SS).

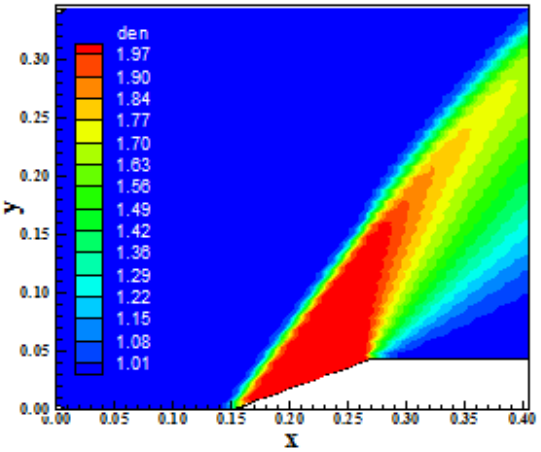

Figure 11: Density Field ([2] – AS).

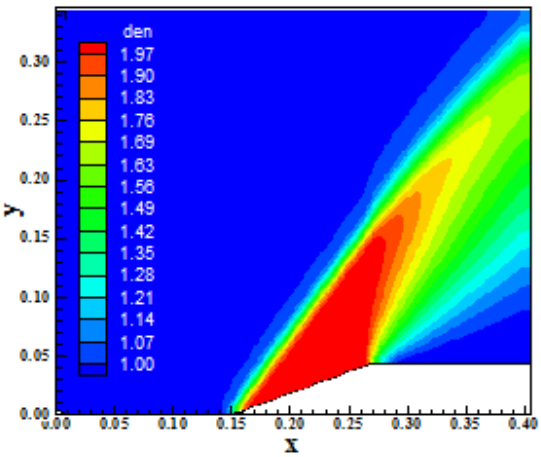

Figure 12: Density Field ([4] – SS).

One way to quantitatively verify if the solutions to the ramp problem are satisfactory consists in determining the shock angle of the oblique shock

wave, β, measured in relation to the initial direction of the flow field, obtained by each scheme. [47] (pages 352 and 353) presents a diagram with values of the shock angle, β, to oblique shock waves.

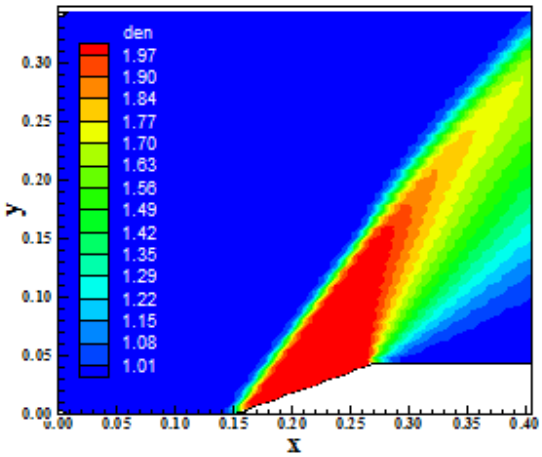

Figure 13: Density Field ([4] – AS).

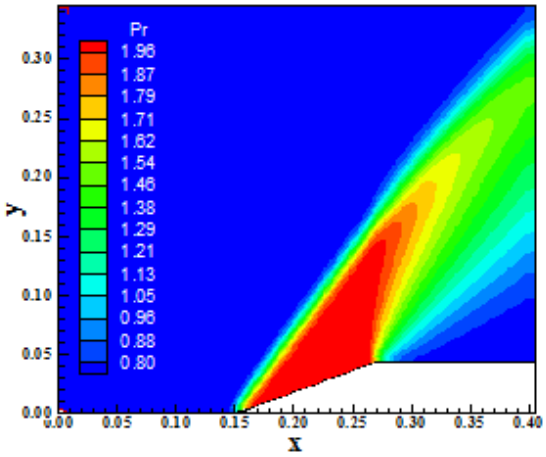

Figure 14: Pressure Field ([2] – SS).

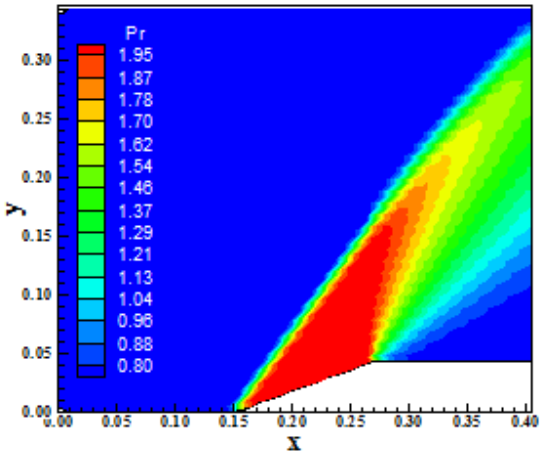

Figure 15: Pressure Field ([2] – AS).

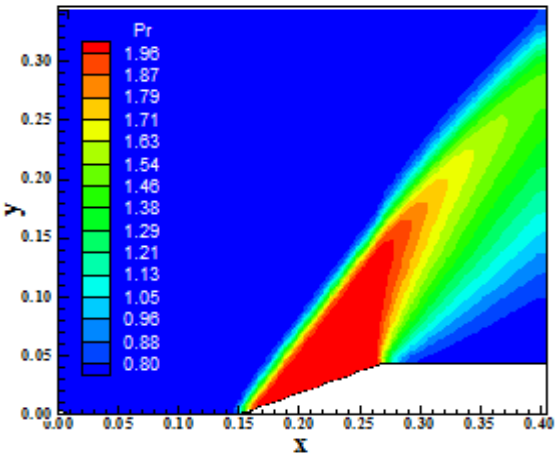

Figure 16: Pressure Field ([4] – SS).

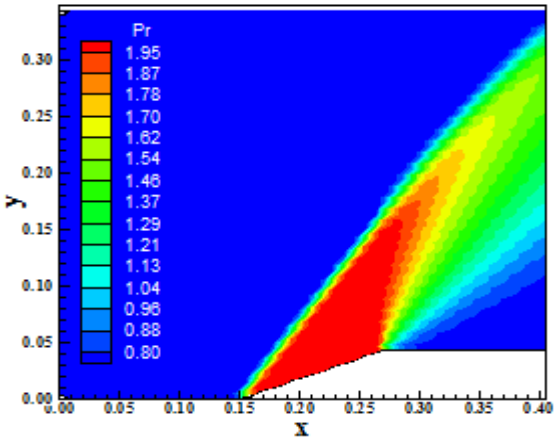

Figure 17: Pressure Field ([4] – AS).

The value of this angle is determined as function of the freestream Mach number and of the deflection angle of the flow after the shock wave, ϕ. To ϕ = 20º (ramp inclination angle) and to a freestream Mach number equals to 2.0, it is possible to obtain from this diagram a value to β equals to 53.0 º. Using a transfer in Figures 14 to 17, it is possible to obtain in Tab. 4:

Algorithm:	β (°):	Error (%):
[2] – SS	55.0	3.77
[2] – AS	53.4	0.75
[4] – SS	53.8	1.51
[4] – AS	53.6	1.13

Table 4: Shock Angle and Percentage Error to the Ramp Problem – First Order.

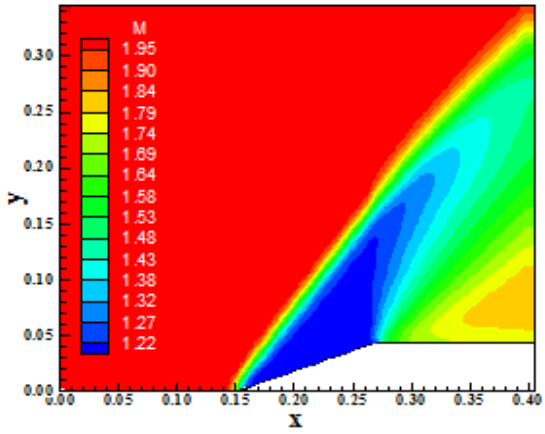

Figure 18: Mach Number Field ([2] – SS).

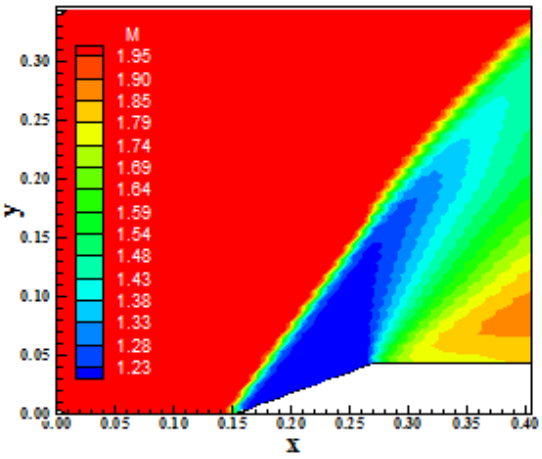

Figure 19: Mach Number Field ([2] – AS).

The percentage errors indicate the [2] scheme and the AS case as more accurate than the other ones in the estimation of the shock angle of the oblique shock wave, considering first order solutions.

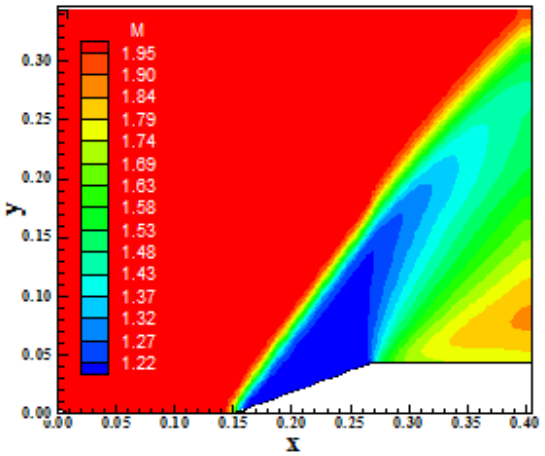

Figure 20: Mach Number Field ([4] – SS).

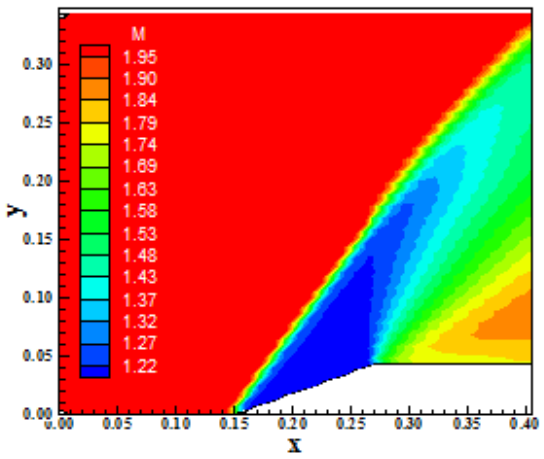

Figure 21: Mach Number Field ([4] – AS).

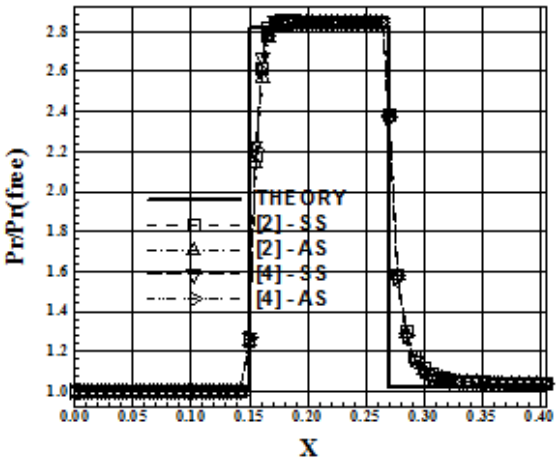

Figure 22: Wall Pressure Distribution.

Figure 22 shows the pressure distributions along the ramp obtained by the [2] and [4] first order schemes, to the SS and AS cases. They are compared with the oblique shock wave and the Prandtl-Meyer expansion wave theories. The shock and the expansion fan are appropriately formed and well solved by all schemes. The pressure plateau is better predicted by [4] scheme, considering the AS case. All algorithms capture appropriately the shock discontinuity within three (3) points. The expansion-fan-end pressure is well detected by all schemes.

By the obtained results, for the first order solutions, the [4] scheme considering the AS case presents the best wall pressure distribution, whereas the [2] scheme considering also the AS case presents the best prediction of the shock angle of the oblique shock wave.

10.2 Second Order Inviscid Solutions – Ramp Problem

In this section, the second order versions of the [2] and [4] algorithms are presented. Five (5) non-linear limiters, which incorporate TVD properties to the numerical schemes, were tested, but only three (3) yielded converged solutions, in general. The three non-linear limiters that yielded converged results were: Barth and Jespersen, Van Leer and Van Albada. Only the Van Leer non-linear limiter did not produce converged results as the [4] scheme, in the SS case, was studied. To facilitate the non-linear limiters nomenclature, they were abbreviated by: BJ (Barth and Jespersen), VL (Van Leer) and VA (Van Albada). The results follow the aforementioned order.

10.2.1 Barth and Jespersen non-linear limiter solutions

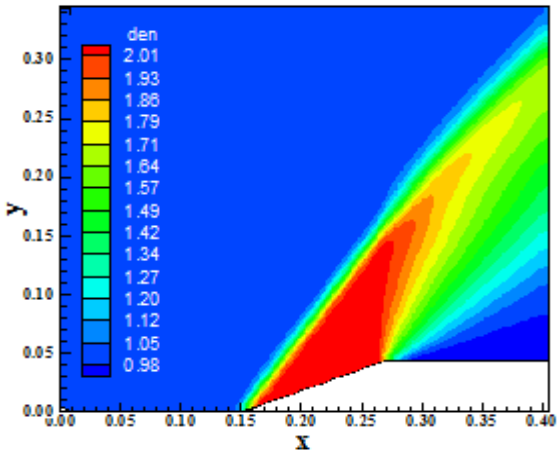

Figure 23: Density Field ([2] – SS).

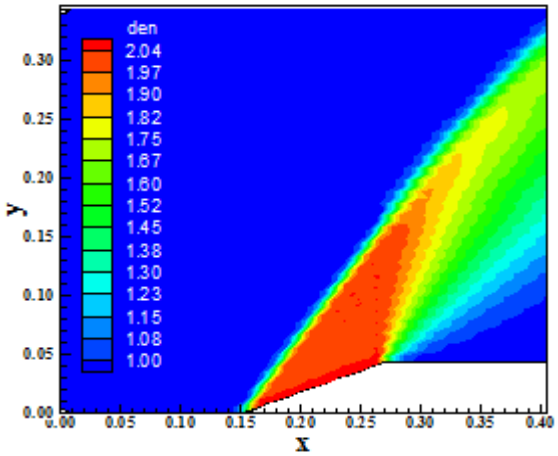

Figure 24: Density Field ([2] – AS).

Figures 23 to 26 present the density field calculated by [2] and [4], in cases SS and AS, as using the BJ non-linear limiter. As can be observed, the density field obtained by the [4] algorithm in the AS case exhibits the densest field. As also can be observed, the AS cases yielded the smallest shock wave thickness, similarly to the first-order-solution behavior.

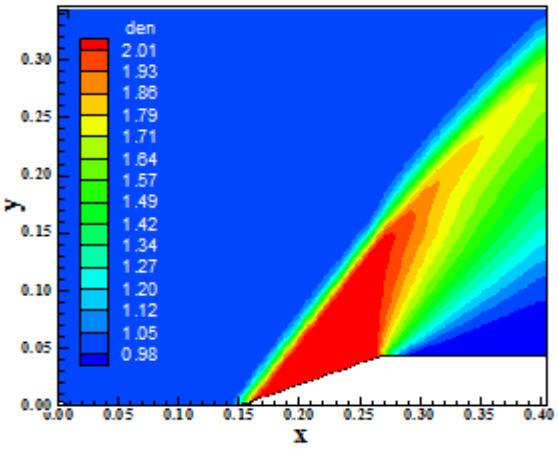

Figure 25: Density Field ([4] – SS).

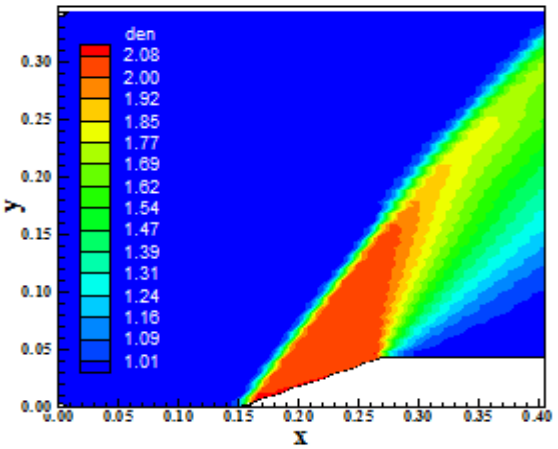

Figure 26: Density Field ([4] – AS).

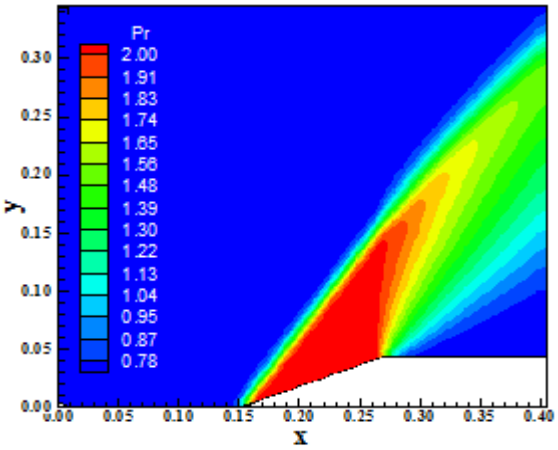

Figure 27: Pressure Field ([2] – SS).

Figures 27 to 30 show the pressure field obtained by [2] and [4] in cases SS and AS. The most severe

pressure field is obtained by [4] in the AS case. The smallest shock wave thickness are again observed in the AS cases. These cases also present the "cut out" effect, which is characteristic of the type of spatial discretization. It is also possible to note in Fig. 30 that the shock region downstream the ramp presents some oscillations, which indicate a non-uniform plateau at the ramp region.

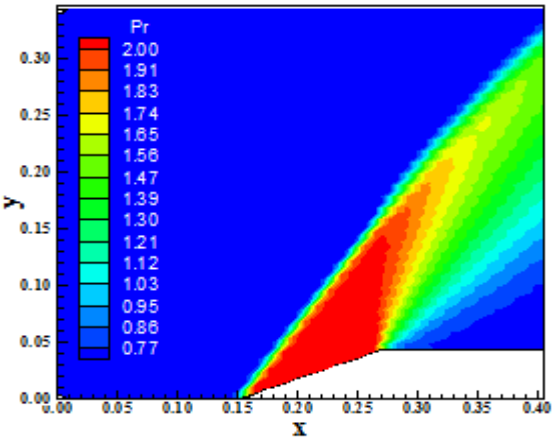

Figure 28: Pressure Field ([2] – AS).

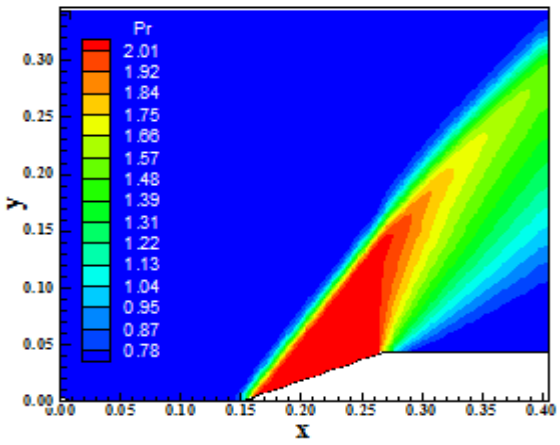

Figure 29: Pressure Field ([4] – SS).

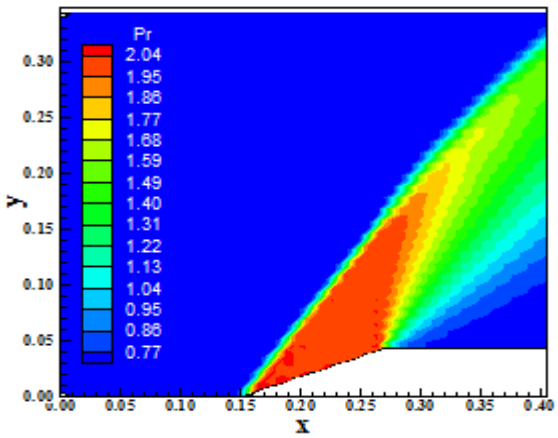

Figure 30. Pressure Field ([4] – AS).

Figures 31 to 34 exhibit the Mach number field generated by [2] and [4] in the cases SS and AS. The most intense Mach number field is obtained by the [2] algorithm, in the AS case. As can be seen, some Mach number oscillations are present along the shock wave in the AS solutions.

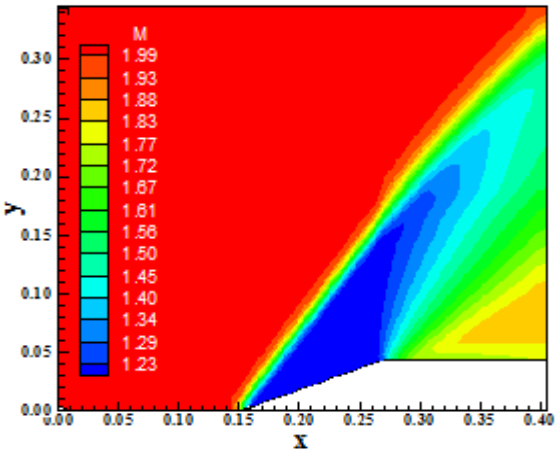

Figure 31: Mach Number Field ([2] – SS).

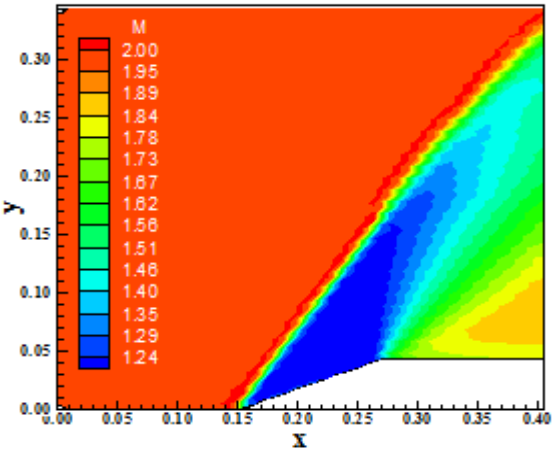

Figure 32: Mach Number Field ([2] – AS).

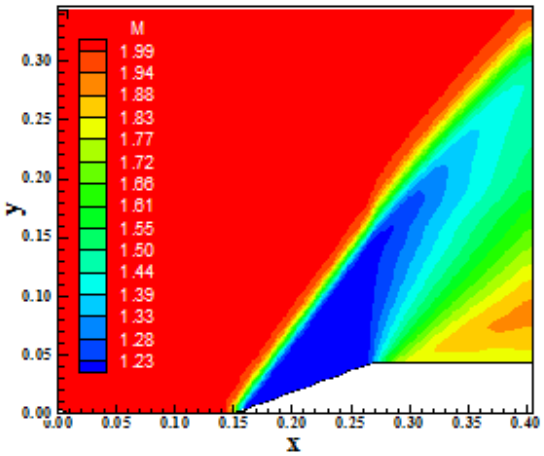

Figure 33: Mach Number Field ([4] – SS).

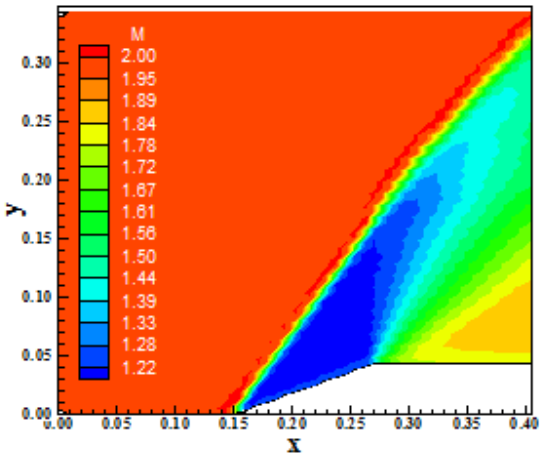

Figure 34: Mach Number Field ([4] – AS).

Figure 35 shows the wall pressure distribution obtained by [2] and [4], as using the BJ non-linear limiter, in the cases SS and AS. This pressure distribution is compared with the oblique shock wave and expansion wave theories. As can be visualized, the best solution is due to [4] in the SS case. It is also observed that all distributions present a pressure peak at the beginning of the ramp. It is also important to note that both SS solutions predict the expansion-fan-pressure recovery correctly. All solutions capture the shock discontinuity in four (4) points, worse than the first order solutions.

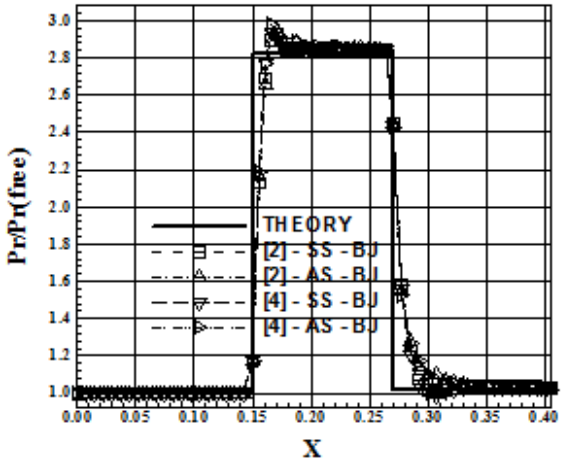

Figure 35: Wall Pressure Distribution.

In relation to the shock angle of the oblique shock wave, the estimation for this parameter to each algorithm and case is presented in Tab. 5. Using a transfer in Figs. 27 to 30, it is possible to obtain the following results. The percentage errors indicate the [2] scheme and the AS case as more accurate than the other ones in the determination of the shock angle of the oblique shock wave, considering the second order solutions of BJ non-linear limiter.

Algorithm:	β (°):	Error (%):
[2] – SS	54.0	1.89
[2] – AS	53.3	0.57
[4] – SS	54.0	1.89
[4] – AS	53.8	1.51

Table 5: Shock Angle and Percentage Error to the Ramp Problem – Second Order (BJ).

10.2.2 Van Leer non-linear limiter Solutions

The second studied non-linear limiter was the Van Leer one. Figures 36 to 38 presents the density field obtained by [2] and [4] algorithms in SS and AS cases. Only the [4] solution in the SS case did not present converged results. As can be seen, the AS solutions present the smallest shock wave thickness. The "cut out" effect of these solutions is again observed. The [4] scheme in the AS case presents the densest field, although the solution quality is not the best. As can be observed until now, although the SS case exhibit better quality of the property contours, the AS case exhibit better shock wave thickness prediction, as also the best shock angle of the oblique shock wave. It seems that the fact of changing the unstructured discretization from one row to the other, alternating the sense of triangulation, incorporates better properties in the mesh, resulting in solutions more accurate. This behavior will be clearer in the viscous case.

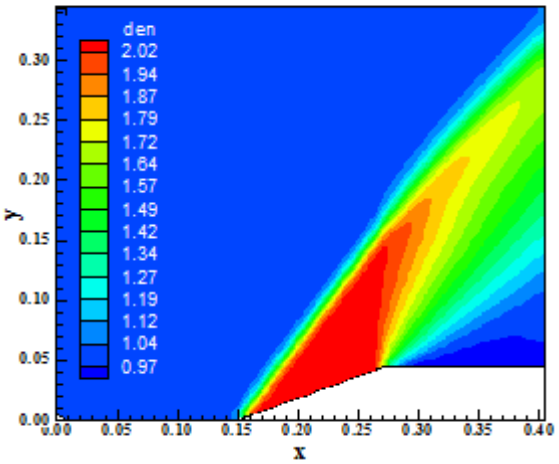

Figure 36: Density Field ([2] – SS).

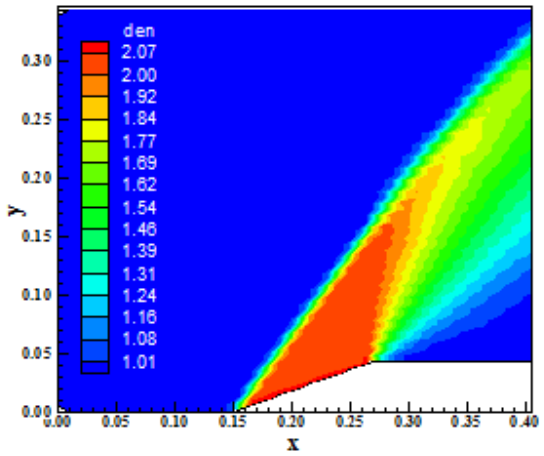

Figure 37: Density Field ([2] – AS).

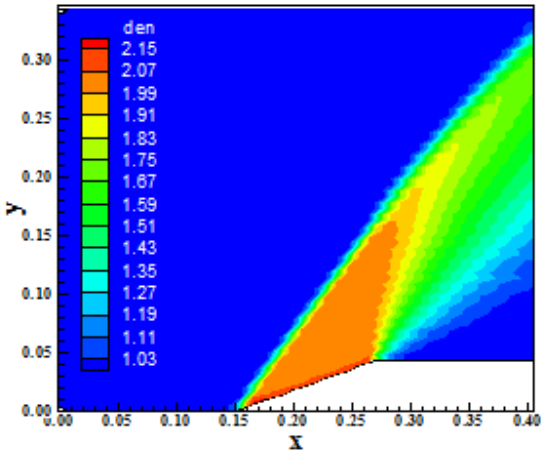

Figure 38: Density Field ([4] – AS).

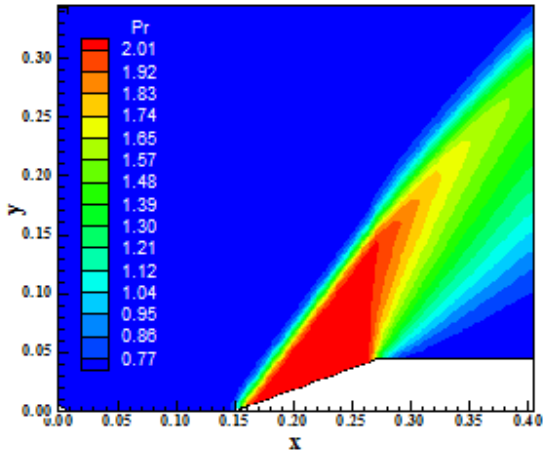

Figure 39: Pressure Field ([2] – SS).

Figures 39 to 41 show the pressure field generated by [2] and [4] in cases SS and AS. Only the [4] algorithm in the SS case did not present converged solution. The most severe pressure field is obtained by the [4] scheme in the AS case, which characterizes this algorithm and case as the most conservative. Figure 41 presents a pressure peak close to the ramp beginning. It will originate a peak at the wall pressure distribution and possibly Mach number oscillations in this region. It is also important to emphasize the smallest thickness of the AS cases. It seems that the alternate sense in the unstructured discretization allows the numerical schemes to capture better shock wave properties. It seems that the discretization error in one row is canceled by the following row.

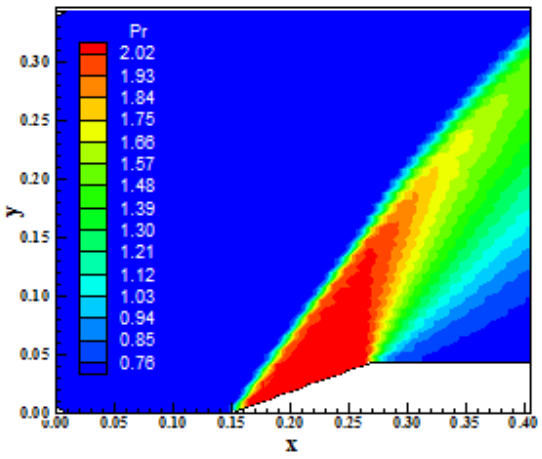

Figure 40: Pressure Field ([2] – AS).

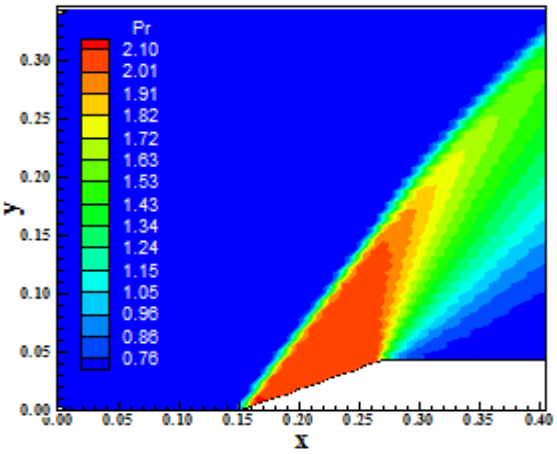

Figure 41. Pressure Field ([4] – AS).

Figures 42 to 44 exhibit the Mach number field generated by the [2] and [4] algorithms. They are analyzed considering the SS and AS cases. All contour solutions present a small oscillation at the ramp beginning, which does the maximum Mach number field bigger than the initial freestream Mach number distribution. Despite it, all solutions are of good quality and clear. The maximum Mach number field is due to [2] in the AS case. The shock resolution is improved by the use of the AS unstructured spatial discretization. In spite of the

"cut out" effect, these solutions are the most representative of the field properties. This problem is classical in the CFD community and is used to simulate for instance the "boosters" of the VLS (Brazilian Satellite Launcher Vehicle) in a first stage of project phase.

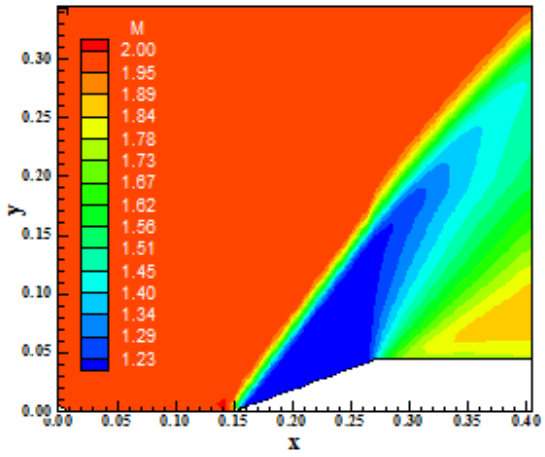

Figure 42: Mach Number Field ([2] – SS).

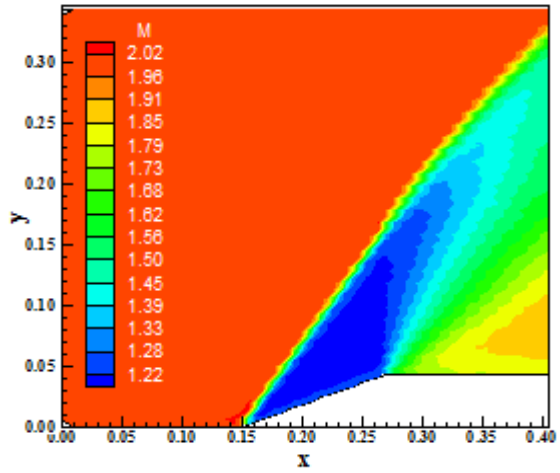

Figure 43: Mach Number Field ([2] – AS).

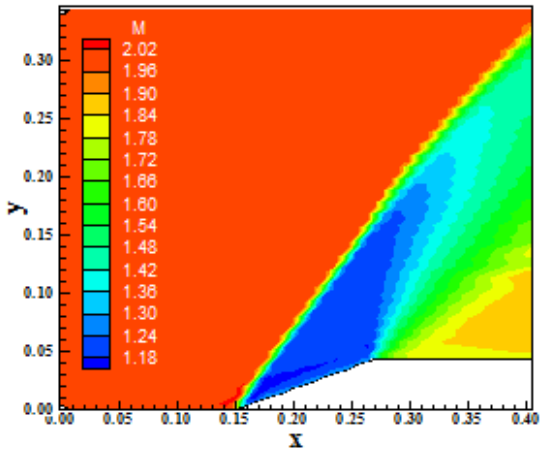

Figure 44: Mach Number Field ([4] – AS).

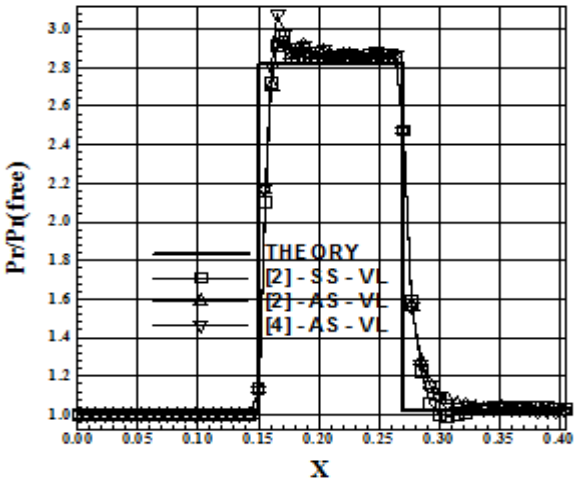

Figure 45: Wall Pressure Distribution.

Figure 45 shows the wall pressure distribution obtained by the [2] algorithm, in cases SS and AS, and the [4], in case AS. As can be seen, all distributions present a peak at the ramp beginning. All solutions capture the shock discontinuity within four (4) points. The closest solution, in relation to the theoretical result, is that generated by the [2] scheme and the SS case. However, the closest expansion-fan-pressure recovery is obtained by the [2] and [4] algorithms in the AS case.

In relation to the shock angle of the oblique shock wave, the estimation for this parameter to each algorithm and case is presented in Tab. 6. Using a transfer in Figs. 39 to 41, it is possible to obtain the following results. The percentage errors indicate the [4] scheme and the AS case as more accurate than the other ones in the determination of the shock angle of the oblique shock wave, considering the second order solutions of Van Leer.

Algorithm:	β (°):	Error (%):
[2] – SS	52.9	0.19
[2] – AS	53.7	1.32
[4] – AS	53.0	0.00

Table 6: Shock Angle and Percentage Error to the Ramp Problem – Second Order (VL).

2.2.3 Van Albada non-linear limiter Solutions

The last non-linear limiter which produced converged results is the Van Albada one. Figures 46 to 49 exhibit the density field obtained by [2] and [4] in cases SS and AS. Comparing these figures, it is possible to distinguish the [4] scheme in the AS

case as the densest field. However, the shock region is full of density oscillations. In Figure 47, some density oscillations appear, following the shock profile. The best solution qualities are obtained in the SS cases.

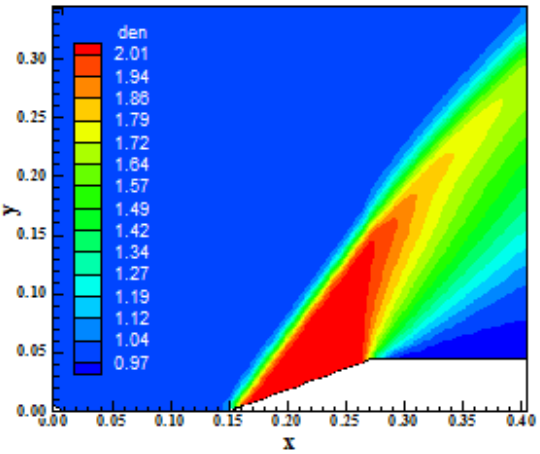

Figure 46: Density Field ([2] – SS).

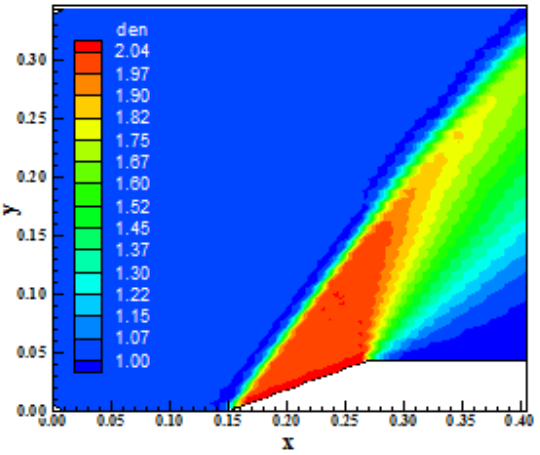

Figure 47: Density Field ([2] – AS).

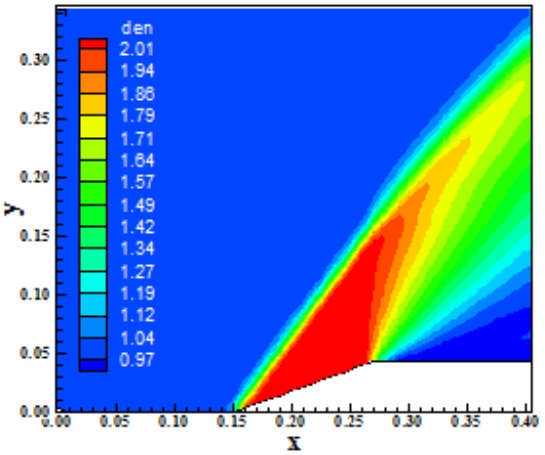

Figure 48: Density Field ([4] – SS).

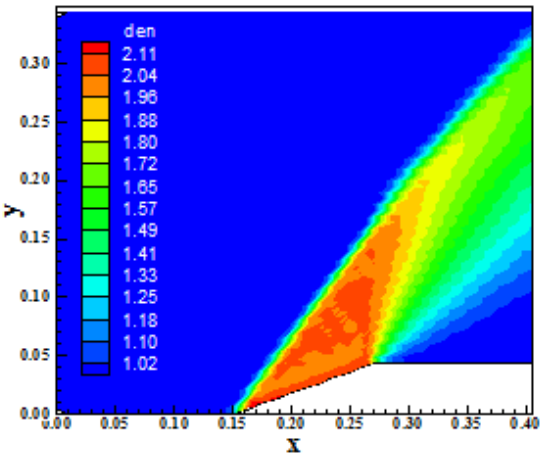

Figure 49: Density Field ([4] – AS).

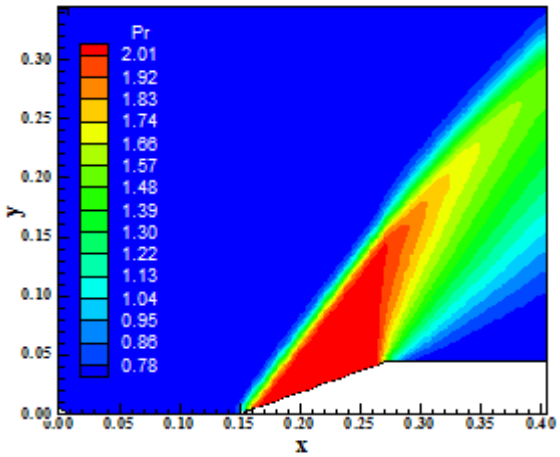

Figure 50: Pressure Field ([2] – SS).

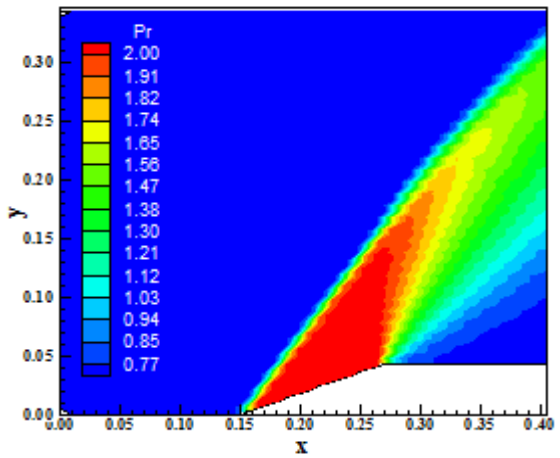

Figure 51: Pressure Field ([2] – AS).

Figures 50 to 53 exhibit the pressure field generated by the [2] and [4] algorithms in the SS and AS cases. As observed, the most severe pressure field is obtained by [4] scheme in the AS case. However, a pressure oscillation is found at the ramp

beginning, which originates a pressure peak in the wall pressure distribution. The smallest shock wave thickness is observed again in the AS cases.

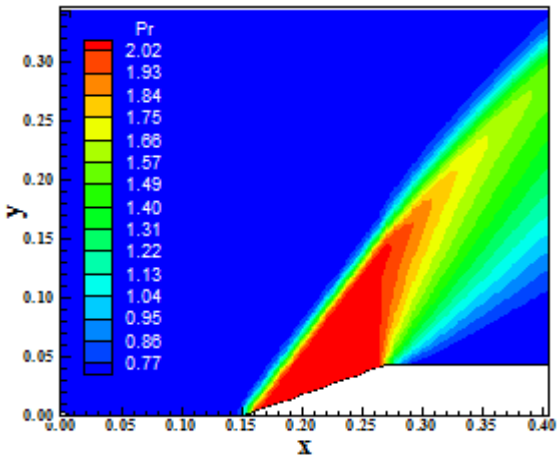

Figure 52: Pressure Field ([4] – SS).

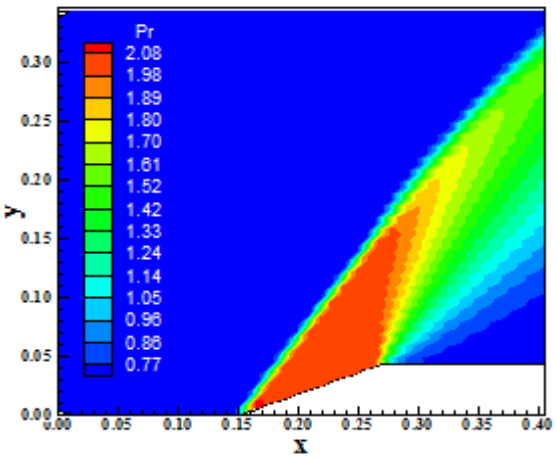

Figure 53: Pressure Field ([4] – AS).

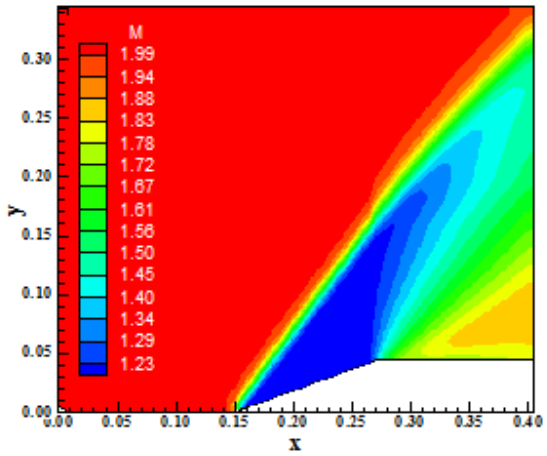

Figure 54: Mach Number Field ([2] – SS).

Figures 54 to 57 show the Mach number field obtained by the [2] and [4] schemes in the SS and AS cases. The most intense Mach number field is generated by [2] scheme in AS case. Both AS cases present Mach number oscillations at the ramp beginning, which is a non-physical situation.

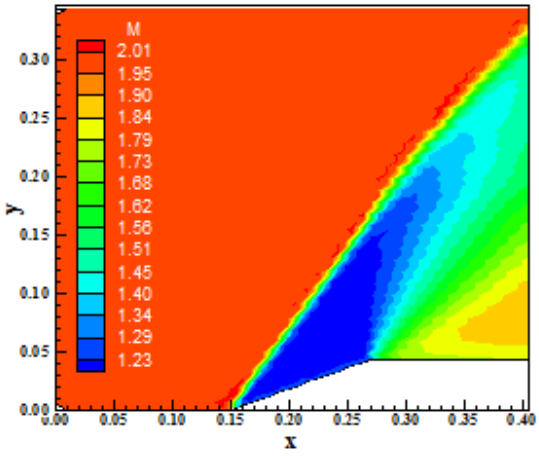

Figure 55: Mach Number Field ([2] – AS).

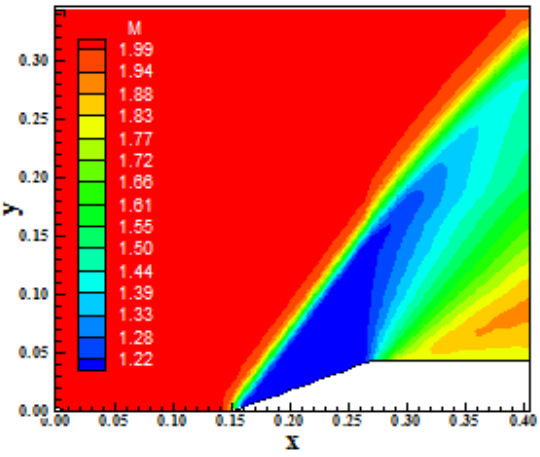

Figure 56: Mach Number Field ([4] – SS).

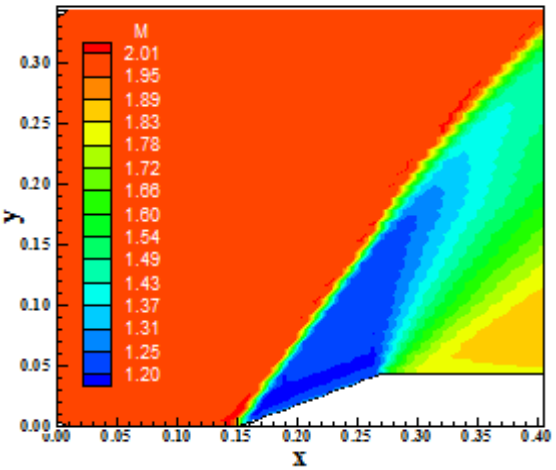

Figure 57: Mach Number Field ([4] – AS).

Figure 58 exhibits the wall pressure distribution generated by the [2] and [4] schemes in the SS and AS cases. All solutions capture the chock discontinuity in four (4) points. All solutions also present a pressure peak at the ramp beginning. The best wall pressure distribution is due to [4] in the SS case. Even with the oscillation, this scheme is closer to the theoretical results than the others. Both AS solutions present better expansion-fan-pressure recovery

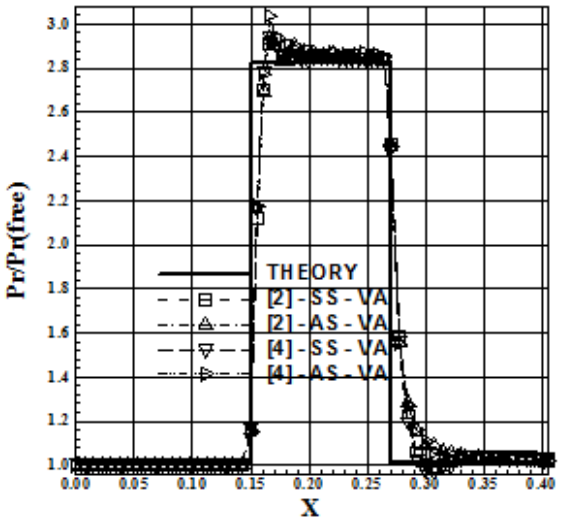

Figure 58: Wall Pressure Distribution.

In relation to the shock angle, Table 7 presents the results in the estimation of this parameter. As can be seen, the best result is proportioned by the [4] algorithm in the case SS. It is also important to note that all errors were inferior to 1.0%, which indicates that the Van Albada non-linear limiter presented the best behavior among the tested ones.

Algorithm:	β (°):	Error (%):
[2] – SS	53.3	0.57
[2] – AS	53.4	0.75
[4] – SS	53.0	0.00
[4] – AS	53.2	0.38

Table 7. Shock Angle and Percentage Error to the Ramp Problem – Second Order (VA).

10.3 Time Step Study

In this work were studied five types of time step: four (4) to inviscid flows and one (1) to viscous flows. The viscous-flow-time-step option is analyzed in the next paper of this work (see [46]). In this paper only the inviscid options are evaluated. Table 8 gives the maximum number of CFL, the number of iterations to obtain convergence and the computational cost to each time step option. The [2] algorithm, in its first order variant, was employed in the numerical experiments.

Time Step Option:	CFL:	Number of Iterations:	Cost[(1)]:
Constant time step	1.30	684	0.0000181
Convective time step	1.10	618	0.0000187
Geometrical 1 time step	65.00	685	0.0000182
Geometrical 2 time step	0.04[(2)]	711	0.0000189

[(1)]: Gives in seconds/per iteration/per cell; [(2)]: exp = 0.33.

Table 8: Characteristics of the Time Step Options.

As pointed out above the best convergence is obtained by the convective time step option, being only 3.31% most expensive than it contra part the constant time step option. The geometrical 1 time step option also is a good procedure to accelerate the convergence process, being only 0.55% more expensive than the constant time step option.

As conclusion, for inviscid cases, the convective time step as implemented in this work involves the best cost-benefit relation and is the recommended procedure to this type of flow. Similar result was obtained in [21-22].

10.4 Computational Cost of the Numerical Schemes

Table 9 exhibits the computational cost of the numerical schemes studied in this work. They are given in seconds/per cell/per iteration. As can be seen, the cheapest scheme is the [2] algorithm, in the AS case, first order accurate, using a CFL number of 0.9 and having a computational cost of 0.0000171sec/per cell/per iteration.

Scheme:	Case:	Order:	CFL:	Cost[(1)]:
[2]	SS	1st	0.9	0.0000172
[2]	SS	2nd – BJ	0.1	0.0002051
[2]	SS	2nd – VL	0.1	0.0002035
[2]	SS	2nd – VA	0.1	0.0002038
[2]	AS	1st	0.9	0.0000171
[2]	AS	2nd – BJ	0.1	0.0002013
[2]	AS	2nd – VL	0.1	0.0002020
[2]	AS	2nd – VA	0.1	0.0002036
[4]	SS	1st	0.9	0.0000178
[4]	SS	2nd – BJ	0.1	0.0002010
[4]	SS	2nd – VA	0.1	0.0002021
[4]	AS	1st	0.9	0.0000177
[4]	AS	2nd – BJ	0.1	0.0002022
[4]	AS	2nd – VL	0.1	0.0002029
[4]	AS	2nd – VA	0.1	0.0002011

(1): Gives in seconds/per iteration/per cell

Table 9: Computational Cost of the Numerical Schemes.

11 Conclusions

In this work, numerical simulations involving supersonic and hypersonic flows on an unstructured context are analyzed. Based on the experiences performed in the structured and unstructured contexts, the [2] and [4] algorithms are implemented on a finite volume formulation, using unstructured spatial discretization. The algorithms are implemented in their first and second order spatial accuracies. The second order spatial accuracy is obtained by a linear reconstruction procedure based on the work of [9]. Several non-linear limiters are studied, as well two types of linear interpolation, based on the works of [18] and [34]. Two types of viscous calculation to the laminar case are compared. They are programmed considering the works of [34] and [35]. To the turbulent simulations, the k-ω^2 two-equation model of [33] is employed, considering the good experience observed by the present author in the structured studies. The ramp problem in the supersonic inviscid case and the re-entry capsule problem in the hypersonic viscous case are considered. A spatially variable time step procedure is implemented aiming to obtain fast convergence rates to the two algorithms, as reported by [21-22]. Five options of time step are described and studied. The results have demonstrated that the [2] algorithm yields the best result in terms of the prediction of the shock angle of the oblique shock wave in the ramp problem and the best value of the stagnation pressure at the configuration nose of the re-entry capsule problem. In terms of turbulent results, the [33] model yields good results, proving the good capacity of this turbulence model to simulate high hypersonic flows.

In terms of the time step options to simulate supersonic and hypersonic flows, four (4) options were employed to study the ramp problem in inviscid conditions. The results presented in Tab. 8 indicate the convective time step as the best technique to accelerate the convergence of numerical algorithms to the steady state solution, according to [21-22].

The cheapest scheme is the [2] algorithm, in the AS case, first order accurate, using a CFL number of 0.9 and presenting a computational cost of 0.0000171sec/per cell/per iteration.

This paper is the first part of this study and treats exclusively with the theory employed in this work and the inviscid results. The laminar and turbulent viscous results and their analyses are the subject of the second paper of this study and are reported in [46].

12 Acknowledgments

The present author acknowledges the CNPq by the financial support conceded under the form of a DTI (Industrial Technological Development) scholarship no. 384681/2011-5. He also acknowledges the infra-structure of the ITA that allowed the realization of this work.

References:

[1] P. Kutler, Computation of Three-Dimensional, Inviscid Supersonic Flows, *Lecture Notes in Physics*, Vol. 41, 1975, pp. 287-374.

[2] B. Van Leer, Flux-Vector Splitting for the Euler Equations, Proceedings of the 8th International Conference on Numerical Methods in Fluid Dynamics, E. Krause, Editor, *Lecture Notes in*

Physics, Vol. 170, 1982, pp. 507-512, Springer-Verlag, Berlin.

[3] M. Liou, and C. J. Steffen Jr., A New Flux Splitting Scheme, *Journal of Computational Physics*, Vol. 107, 1993, pp. 23-39.

[4] R. Radespiel, and N. Kroll, Accurate Flux Vector Splitting for Shocks and Shear Layers, *Journal of Computational Physics*, Vol. 121, 1995, pp. 66-78.

[5] P. L. Roe, Approximate Riemann Solvers, Parameter Vectors, and Difference Schemes, Journal of Computational Physics, Vol. 43, 1981, pp. 357-372.

[6] E. Turkel, and B. Van Leer, Flux-Vector Splitting and Runge-Kutta Methods for the Euler Equations, *ICASE Report 84-27*; also *NASA CR 172415*, 1984.

[7] D. W. Riggins, R. W. Walters, and D. Pelletier, The use of Direct Solvers for Compressible Flow Computations, *AIAA Paper 88-0229*, 1988.

[8] D. Mavriplis, and A. Jameson, Multigrid Solution of the Euler Equations on Unstructured and Adaptive Meshes, *ICASE Report 87-53*; also *NASA CR 178346*, 1987.

[9] T. J. Barth, and D. C. Jespersen, The Design and Application of Upwind Schemes on Unstructured Meshes, *AIAA Paper 89-0336*, 1989.

[10] B. Stoufflet, J. Périaux, F. Fezoui, and A. Dervieux, Numerical Simulation of 3-D Hypersonic Euler Flows Around Space Vehicles Using Adapted Finite-Elements, *AIAA Paper 87-0560*, 1987.

[11] D. L. Whitaker, Two-Dimensional Euler Computations on a Triangular Mesh Using an Upwind, Finite-Volume Scheme, *Ph.D. Thesis*, Dept. of Aerospace and Ocean Engineering, Virginia Polytechnic Inst. and State Univ., Blacksburg, VA, 1988.

[12] E. S. G. Maciel, Comparison Between the First Order Upwind Unstructured Algorithms of Roe and of Harten in the Solution of the Euler Equations in Two-Dimensions, *Proceedings of the XIX Congress of Mechanical Engineering (XIX COBEM)*, Brasília, DF, Brazil, 2007.

[13] E. S. G. Maciel, Comparison Between the First Order Upwind Unstructured Algorithms of Steger and Warming and of Van Leer in the Solution of the Euler Equations in Two-Dimensions, *Proceedings of the XIX Congress of Mechanical Engineering (XIX COBEM)*, Brasília, DF, Brazil, 2007.

[14] J. L. Steger, and R. F. Warming, Flux Vector Splitting of the Inviscid Gasdynamic Equations with Application to Finite-Difference Methods, *Journal of Computational Physics*, Vol. 40, 1981, pp. 263-293.

[15] A. Harten, High Resolution Schemes for Hyperbolic Conservation Laws, *Journal of Computational Physics*, Vol. 49, 1983, pp. 357-393.

[16] E. S. G. Maciel, Comparison Among the Unstructured Algorithms of Frink, Parikh and Pirzadeh, of Liou and Steffen, and of Radespiel and Kroll in the Solution of the Euler Equations in 2D - Theory, *Proceedings of the 8th Symposium of Computational Mechanics (VIII SIMMEC)*, Belo Horizonte, MG, Brazil, 2008.

[17] E. S. G. Maciel, Comparison Among the Unstructured Algorithms of Frink, Parikh and Pirzadeh, of Liou and Steffen, and of Radespiel and Kroll in the Solution of the Euler Equations in 2D - Results, *Proceedings of the 8th Symposium of Computational Mechanics (VIII SIMMEC)*, Belo Horizonte, MG, Brazil, 2008.

[18] N. T. Frink, P. Parikh, and S. Pirzadeh, Aerodynamic Analysis of Complex Configurations Using Unstructured Grids, *AIAA 91-3292-CP*, 1991.

[19] E. S. G. Maciel, Extension of the Unstructured Algorithms of Liou and Steffen Jr. and of Radespiel and Kroll to Second Order Accuracy Employing Linear Reconstruction and Application to the Euler Equations in 2D - Theory, *Proceedings of the XX International Congress of Mechanical Engineering (XX COBEM)*, Gramado, RS, Brazil, 2009.

[20] E. S. G. Maciel, Extension of the Unstructured Algorithms of Liou and Steffen Jr. and of Radespiel and Kroll to Second Order Accuracy Employing Linear Reconstruction and Application to the Euler Equations in 2D - Results, *Proceedings of the XX International Congress of Mechanical Engineering (XX COBEM)*, Gramado, RS, Brazil, 2009.

[21] E. S. G. Maciel, Analysis of Convergence Acceleration Techniques Used in Unstructured Algorithms in the Solution of Aeronautical Problems – Part I, *Proceedings of the XVIII International Congress of Mechanical Engineering (XVIII COBEM)*, Ouro Preto, MG, Brazil, 2005.

[22] E. S. G. Maciel, Analysis of Convergence Acceleration Techniques Used in Unstructured Algorithms in the Solution of Aerospace Problems – Part II, *Proceedings of the XII Brazilian Congress of Thermal Engineering and Sciences (XII ENCIT)*, Belo Horizonte, MG, Brazil, 2008.

[23] E. S. G. Maciel, Extensão dos Algoritmos Não Estruturados de Roe e de Van Leer para Segunda Ordem de Precisão Usando Reconstrução Linear e Aplicação às Equações de Euler em 2D – Teoria, *Anales del II Congreso Argentino de Ingeniería Mecánica (II CAIM)*, San Juan, Argentina, 2010.

[24] E. S. G. Maciel, Extensão dos Algoritmos Não Estruturados de Roe e de Van Leer para Segunda Ordem de Precisão Usando Reconstrução Linear e Aplicação às Equações de Euler em 2D – Resultados, *Anales del II Congreso Argentino de Ingeniería Mecánica (II CAIM)*, San Juan, Argentina, 2010.

[25] E. S. G. Maciel, Estudo de Escoamentos Turbulentos Utilizando os Modelos de Cebeci e Smith e de Baldwin e Lomax e Comparação entre os Algoritmos de MacCormack e de Jameson e Mavriplis, *Proceedings of the VII Symposium of Computational Mechanics (VII SIMMEC)*, Araxá, MG, Brazil, 2006.

[26] E. S. G. Maciel, Comparação entre os Modelos de Turbulência de Cebeci e Smith e de Baldwin e Lomax, *Proceedings of the V Spring School of Transition and Turbulence (V EPTT)*, Rio de Janeiro, RJ, Brazil, 2006.

[27] T. Cebeci, and A. M. O. Smith, A Finite-Difference Method for Calculating Compressible Laminar and Turbulent Boundary Layers, *Journal of Basic Engineering, Trans. ASME*, Series B, Vol. 92, 1970, No. 3, pp. 523-535.

[28] B. S. Baldwin, and H. Lomax, Thin Layer Approximation and Algebraic Model for Separated Turbulent Flows, *AIAA Paper 78-257*, 1978.

[29] R. W. MacCormack, The Effect of Viscosity in Hypervelocity Impact Cratering, *AIAA Paper 69-354*, 1969.

[30] A. Jameson, and D. Mavriplis, Finite Volume Solution of the Two-Dimensional Euler Equations on a Regular Triangular Mesh, *AIAA Journal*, Vol. 24, 1986, No. 4, pp. 611-618.

[31] E. S. G. Maciel, Comparison Between the Two-Equation Turbulence Models of Jones and Launder and of Wilcox and Rubesin Applied to Aerospace Problems, *Journal of Mechanical Engineering Research (JMER)*, JMER 11-030, 2011.

[32] W. P. Jones, and B. E. Launder, The Prediction of Laminarization with a Two-Equation Model of Turbulence, International Journal of Heat and Mass Transfer, Vol. 15, 1972, pp. 301-304.

[33] D. C. Wilcox, and M. W. Rubesin, Progress in Turbulence Modeling for Complex Flow Fields Including the Effects of Compressibility, *NASA TP-1517*, 1980.

[34] F. Jacon, and D. Knight, A Navier-Stokes Algorithm for Turbulent Flows Using an Unstructured Grid and Flux Difference Splitting, *AIAA Paper 94-2292*, 1994.

[35] L. N. Long, M. M. S. Khan, and H. T. Sharp, Massively Parallel Three-Dimensional Euler / Navier-Stokes Method, *AIAA Journal*, Vol. 29, 1991, No. 5, pp. 657-666.

[36] R. W. Fox, and McDonald, A. T., *Introdução à Mecânica dos Fluidos*, Ed. Guanabara Koogan, Rio de Janeiro, RJ, Brazil, 632 p, 1988.

[37] D. J. Mavriplis, and A. Jameson, Multigrid Solution of the Navier-Stokes Equations on Triangular Meshes, *AIAA Journal*, Vol. 28, 1990, No. 8, pp. 1415-1425.

[38] A. Harten, J. Hyman, and P. Lax, On Finite-Difference Approximations and Entropy Conditions for Shocks, Comm. Pure Appl. Math., Vol. 29, 1976.

[39] S. P. Spekreijse, Multigrid Solution of the Steady Euler Equations, *Doctoral Thesis*, Deft University of Technology, 1987.

[40] C. Hirsch, Numerical Computation of Internal and External Flows – Computational Methods for Inviscid and Viscous Flows, John Wiley & Sons Ltd, 691 p, 1990.

[41] L. Martinelli, and A. Jameson, Validation of a Multigrid Method for the Reynolds Average Equations, *AIAA Paper 88-0414*, 1988.

[42] R. Rausch, J. Batina, and H. Yang, Spatial Adaption Procedures on Unstructured Meshes for Accurate Unsteady Aerodynamic Flow Computation, *AIAA Paper 91-1106*, 1991.

[43] D. J. Mavriplis, Accurate Multigrid Solution of the Euler Equations on Unstructured and Adaptive Meshes, AIAA Journal, Vol. 28, 1990, No. 2, pp. 213-221.

[44] S., Pirzadeh, Structured Background Grids for Generation of Unstructured Grids by Advancing Front Method, *AIAA Paper 91-3233-CP*, 1991.

[45] E. S. G. Maciel, Simulação Numérica de Escoamentos Supersônicos e Hipersônicos Utilizando Técnicas de Dinâmica dos Fluidos Computacional, Doctoral *Thesis, ITA*, CTA, São José dos Campos, SP, Brazil, 2002.

[46] E. S. G. Maciel, Supersonic and Hypersonic Flows on 2D Unstructured Context: Part II, WSEAS on Fluid Dynamics, *WSEAS 53-670*, 2011.

[47] J. D. Anderson Jr., *Fundamentals of Aerodynamics*, McGraw-Hill, Inc., 1984.